Enhanced electrolytic immersion cooling for thermal crisis mitigation in high-energy-density systems

Inbaoli A[a], Sujith Kumar C S[a,b*], Sandesh S. Chougule[b], Christos N. Markides[b], Jayaraj S[a]

[a] Department of Mechanical Engineering, NIT Calicut, Kerala-673601, India

[b] Clean Energy Processes (CEP) Laboratory, Department of Chemical Engineering, Imperial College London, London SW7 2AZ, United Kingdom

[*]*Corresponding author: sujithcs@nitc.ac.in*

N.B.: This is the ACCEPTED MANUSCRIPT version of this article. The final, published version of the article can be found at https://doi.org/10.1016/j.enconman.2023.117980.

Abstract

Motivated by the increasing need for effective cooling solutions in high-energy-density systems, this experimental study presents the two-phase cooling of a superheated SS 316L sample via immersion quenching in saturated deionized (DI) water at atmospheric pressure conditions with and without a DC electric field. We investigate the effect of the applied electric field, electrode polarity, and in-situ oxidation on quenching characteristics such as the cooling profile, vapour layer behaviour, minimum film boiling temperature (T_{min}), and heat transfer rate. The cooling curves of samples quenched with the application of an electric field shift towards the left compared to the sample quenched without an electric field. The cathode sample at 200 V exhibits 33% faster cooling than the bare sample (0 V). Overall, the in-situ oxidised SS 316L cathode sample at 200 V exhibits a 55% reduction in film boiling duration, and T_{min} increased from 268 °C to 322 °C compared to the bare sample (0 V). The visualisation studies highlight that the liquid-vapour interface experiences a series of oscillations followed by temporal collapse due to electrostatic attraction and electrolytic activity. The obtained results show that hydrogen-rich vapour bubbles increase heat transfer performance. The evolution of hydrogen and its adsorption at the sample surface reduces the activation energy for bubble nucleation and improves the bubble density via liquid pumping. These insights open the pathway for employing hydrogen bubbles for handling ultra-high thermal loads in high-energy density systems, and the specific case of a revised design of concentrating solar receiver is considered based on the present findings.

Keywords: electrolysis, film boiling, hydrogen bubbles, immersion cooling, in-situ oxidation.

1. Introduction

Green and sustainable cooling technologies are vital for health care services, food and nutrition safety, well-being and thermal comfort of humans [1,2] reducing the environmental impact of cooling systems (air conditioning and refrigeration systems) [3,4] and minimizing energy consumption by sustainable and renewable energy systems [5,6]. One of the essential steps toward carbon neutrality in power generation is the development of efficient cooling solutions for sustainable and renewable energy systems. The effectiveness of cooling technologies shapes the innovations in high power density sustainable energy systems such as nuclear reactors, concentrated solar thermal power systems, and fuel cells. Ensuring the efficient cooling (thermal comfort) of the system components is the primary design factor to facilitate their efficient and safer operation [7]. Inefficient cooling/low heat dissipation rate (thermal distress) in these high-density energy systems leads to decreased energy efficiency, increased energy consumption, and carbon footprint [8]. In the worst-case scenario, a lack of efficient cooling can leave an irrevocable impact on the environment. For instance, in nuclear power plants, in the event of an unprotected transient over-power accident, the nuclear fuel rod melts and forms highly radioactive corium debris. Thus, in turn leads to significant heat accumulation inside the reactor core. To avoid any further damage, e.g., complete meltdown of the reactor core and release of radiation into the environment, the accumulated heat must be dissipated rapidly [9,10].

As another example, for direct steam generation, major developments have focused on beam down technologies coupled with point-focusing system [11,12]. They are cost-efficient, has low CO_2 emissions, and mitigates the use of hazardous thermal oil as heat transfer fluids [13,14]. In these systems, concentrated solar energy is transferred directly to solar cavity receiver where it is utilized to produce high quality steam for electricity generation. Here, the overall solar-to-electrical energy conversion primarily depends on the thermal efficiency of the solar receiver [15].

The critical factor that hinders the thermal efficiency (heat dissipation rate) of the receiver is the boiling crises such as film boiling [16]. Under high solar flux conditions, the solar receiver suffers from low heat transfer rate due to the vapour layer formation on the receiver surface, which prevents the direct contact between the receiver and water. As a result of low heat dissipation rate, the input solar thermal energy accumulates in the cavity receiver and causes the material degradation followed by complete breakdown of solar receiver.

To prevent the film boiling, augment the operating capacity and the thermal efficiency of the solar cavity receiver at high solar flux conditions it is crucial to enhance the heat dissipation

rate. Therefore, developing an efficient heat transfer strategy that facilitates enhanced heat dissipation rate at high superheats in sustainable energy systems is paramount and it will be even more crucial in the coming decades as power demand continues to grow.

When faced with such demands, two-phase heat transfer is preferred for heat dissipation at high superheats. Two-phase heat transfer solutions involve two approaches: (i) active liquid circulation such as spray/jet impingement [17-19], flow boiling [20-22], and (ii) immersion cooling [23-25]. Although spray/jet impingement and flow boiling offer higher heat transfer coefficient they inevitably suffer from hydrodynamic instabilities, non-uniform heat transfer coefficient on the heater surface, coolant leakage, and complicated system design with more active functional components requiring significant amount of electrical power (pumping power) to facilitate the cooling process. In contrast, immersion cooling includes simple system design without any complicated moving parts and also energy efficient. Therefore, this study focuses on the immersion cooling method in particular transient cooling as an effective strategy for enhancing the heat dissipation rate at high superheat.

At high superheats the coolant undergoes rapid evaporation to form an insulating vapour layer around the heated surface, which deters the heat transfer rate by cutting off the direct contact of coolant-heated surface This condition is termed film boiling [26]. Two critical parameters of film boiling are minimum film boiling temperature (T_{min}) and vapour layer instability. T_{min} indicates the termination of film boiling, and vapour layer instability dictates the film boiling heat transfer rate. Here, the ultimate objective is to achieve efficient cooling by increasing T_{min} and vapour layer instability.

In this regard, researchers have employed both passive and active heat transfer enhancement techniques. The former involve cooling surface and/or coolant modifications [27], while the latter involve external force fields such as electric or magnetic fields, mechanical agitation, and acoustic vibrations [28]. Ample research focused on developing new coatings [29,30], micro/nanostructures [31,32] to elevate T_{min}. In film boiling, the height of developed nano/microstructures must be higher than the vapour layer thickness; otherwise, the enhancement effect by surface modification is negligible [33]. Further, the structural integrity of developed coating/structures at high temperatures is also a major concern.

On the other hand, the coolant modification approach is limited by operating temperature due to the thermal degradation of additives in the coolant. On the contrary, active approaches have the advantage of not requiring additional sample or coolant modification, although they involve more

complicated system design (e.g., requiring a magnetic field, mechanical agitation, or acoustic vibrations) and can be expensive [34]. Such complications can be avoided using an external electric field for active heat transfer enhancement. So, the present experimental investigation focuses on employing electric fields to enhance the transient heat transfer and T_{min}.

Celestini et al. [35] demonstrated the influence of an electric field to alter the vapour layer behaviour on the Leidenfrost droplet. Later, Shahriari et al. [36] extended this droplet study to immersing quenching experiments. Their experiments involve immersing quenching of SS316, copper, and chromium alloy steel spheres in isopropanol and ethylene glycol at saturation temperature. The applied voltage value was varied from 0 to 2 kV with an interval of 500 V. The results revealed that film boiling duration decreases by 44% in the presence applied DC electric field. This highlights the ability of the electric field to alter the film boiling during quenching in low electrically conductive organic solvents. The major problem with using organic solvents is their low auto-ignition temperature. When exposed to high temperatures, the organic solvents (e.g., ethylene glycol) will catch fire and burn the entire system. Further, their study overlooked the effect of electrode polarity, oxidation, and surface characteristics on film boiling behaviour.

It is now a well an established proposition that surface oxidation during steady-state pool boiling enhances the boiling heat transfer [37]. However, surface oxidation during transient boiling, particularly on steel substrate, provides no such benefit as improvement in T_{min} [38,39]. Some studies have discussed the effect of electric field on the heat transfer enhancement in steady-state pool boiling experiments [40,41]. However, these studies focus mainly on the heat transfer aspect in the nucleate boiling regime, which provides a very limited understanding of bubble dynamics in electric field assisted film and transition boiling regimes. Thus, it leaves many unanswered questions. For instance, what is the influence of electrode polarity on the minimum film boiling temperature (T_{min})? Can in-situ oxidation enhance the T_{min} in electric field assisted quenching? Does electrolysis always have a positive effect on quenching heat transfer? How do hydrogen-rich vapour bubbles propel the quenching heat transfer? Answering these questions is of greater practical importance and valuable knowledge addition. In this current work, we experimentally investigate the effect of the DC electric field on immersion quenching of SS316L in DI water at saturated conditions under atmospheric pressure. We explore the effects of DC electric field, electrode polarity, and in-situ surface oxidation on vapour layer behaviour, T_{min}, cooling rate, and heat flux characteristics.

2. Experimental methods

In this study, quenching experiments were conducted at two different configurations: without electric field and with electric field. The heat dissipation at the sample surface is analysed via cooling profile and vapour film behaviour via high-speed visualization. The following sections details the test sample preparation, experimental setup and procedure.

2.1 Test sample preparation

Commercially available SS 316L was selected owing to its wide range of applications. The XRD pattern displayed in Fig. 1a shows the sharp diffraction peaks at 2θ = 43.6˚ (111), 50.9˚ (200), 74.7˚ (220). This confirms that the bulk material is the austenitic SS 316L alloy. Fig. 1b shows the details of the test sample used for the quenching experiments. SS 316L cylindrical rod of 10 mm diameter and 60 mm length was selected for this study.

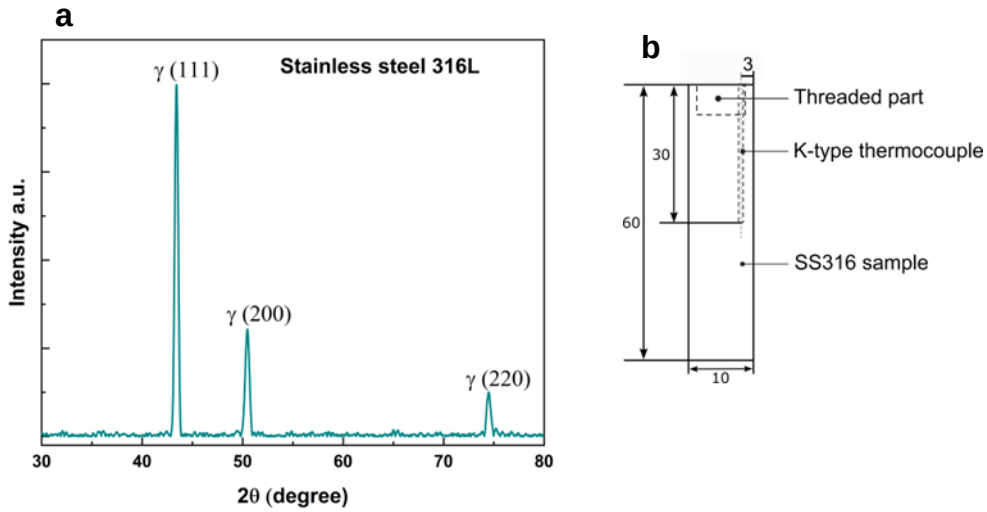

Fig. 1. (a) XRD pattern of SS 316L, and (b) sample dimensions. All dimensions are in mm.

Threading on top of the sample was done to attach the sample to the holder. From the top end of the sample, a blind hole of 0.6 mm diameter was drilled to mount the thermocouple, as shown in Fig. 1b. Prior to the experiments, the samples were polished using sandpapers of different grades from #400 - #2000. Then the polished workpiece was ultra-sonicated using acetone to remove any adhered contaminants for 30 minutes, followed by 30 min of ultra-sonication in DI water. After that, the workpiece was kept in the oven for 2 hr to remove the moisture content.

2.2 Experimental facility

The schematic diagram of the experimental setup used for conducting the quenching experiments with and without an electric field is shown in Fig. 2a.

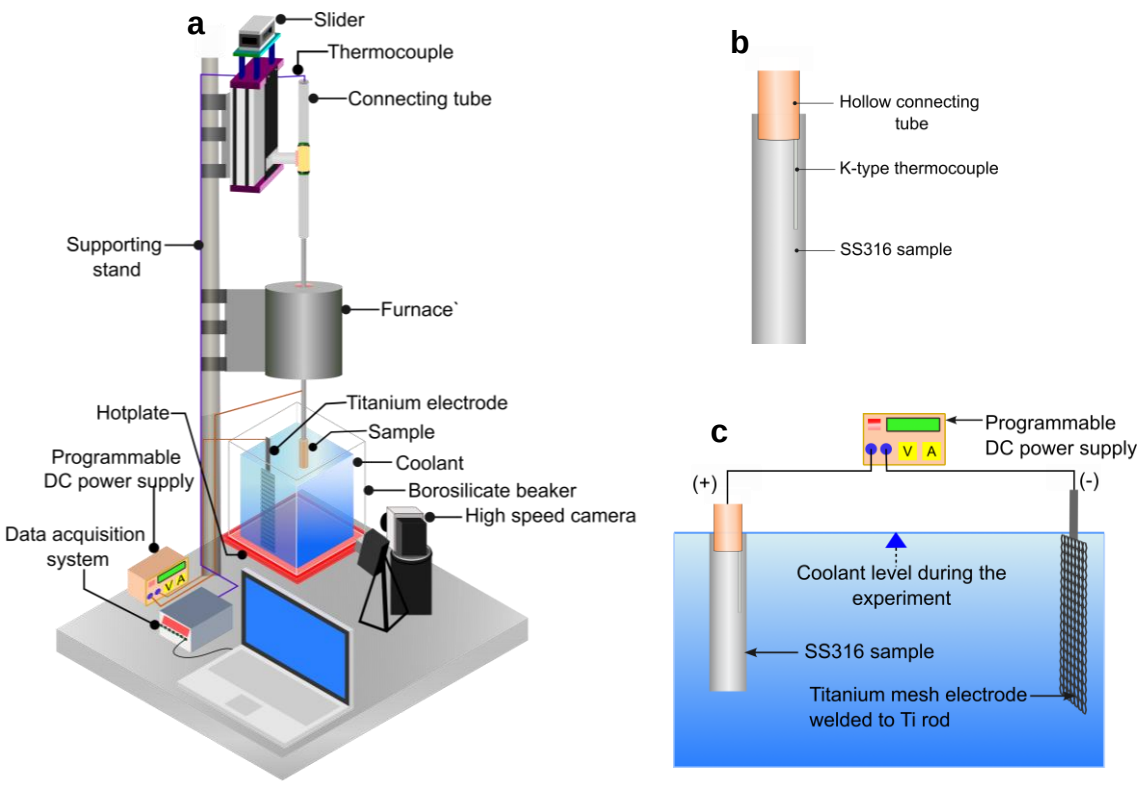

Fig. 2. (a) Schematic diagram of the experimental setup used for conducting the quenching experiments with and without electric field, (b) thermocouple placement inside the sample, and (c) test section showing the electrodes arrangement.

The experimental setup consists of the ceramic furnace (customized), programmable electronic slider (customized), data acquisition system (National Instruments, NI9212), DC voltage source (Scientific Instruments, DC), a hot plate, coolant bath, and high-speed camera (PHANTOM, MIRO LAB110). The ceramic tubular furnace with a maximum temperature of 900 °C was used for radiative heating of the sample. The furnace temperature was regulated using a PID controller coupled with the temperature sensors (k-type thermocouples) mounted inside the furnace. The sample attached to the tail end of the stainless-steel sample holder was hung inside the furnace to heat it to the desired temperature. The front end of the sample holder was mounted to an electronic slider. The programmable single-axis vertical slider was used to immerse the sample into the coolant at a sufficiently high speed of 200 mm/s to avoid radiation heat losses. The limit switches and rails ensured the smooth plunging and positioning of the sample into the coolant bath without vibrations and other motion perturbations.

Mineral insulated ungrounded k-type thermocouple (Tempsens make, maximum uncertainty of ± 0.5 °C at 600 °C) of 0.5 mm probe diameter was employed to obtain the temperature data throughout the experiment. The selected thermocouple avoids the electric interference created

due to the application of an external DC electric field at the output. The thermocouple was connected to NI 9212 data acquisition unit interface with LabView for monitoring and recording the temperature data. The sampling frequency was fixed to 100 Hz in accordance with the minimum response time of the thermocouple (0.07 s as per the manufacturer's specification). The high-temperature thermal conductive paste was applied between the sample and the tip of the thermocouple to avoid thermal resistance. Fig. 2b illustrates the thermocouple in the blind hole drilled in the sample to measure the near-surface temperature during the quenching experiments. More detailed information about the experimental setup can be found elsewhere [42].

An external DC source (max 500 V at 0.1 A) was used to supply the electric potential to the sample during the quenching. The voltage and current were measured using the VI acquisition system at the sampling frequency of 100 Hz. The sample was connected to the anode or cathode terminal, while the other terminal was connected to the counter electrode (see Fig. 2c). Titanium Gr.1ASTM B 265 of 0.9 mm thick with w-type mesh (150 mm length × 50 mm width) and hook (100 mm length × 20 mm width × 1.5 mm thick) was selected as the counter electrode. The mesh-type electrode was chosen because of the high surface-to-area ratio. During quenching, the Ti electrode was positioned to be at a distance of 10 cm from the sample, and both were placed in the coolant bath. A 2.5 L borosilicate glass container was used as the coolant bath, and DI water was selected as the working fluid. DI water was heated to saturation temperature using the plate heater, and its temperature was measured at three locations using k-type thermocouples connected to a data acquisition system. A PHANTOM- MIRO LAB110 high-speed camera with a maximum resolution of 1280 × 800 with 3000 fps was employed to visualize the vapour layer behaviour and bubble dynamics. The visualization videos were recorded through the transparent glass wall of the bath in such a way that the recording axis was perpendicular to the sample. The camera and sample were kept approximately 200 mm apart.

2.3 Experiment procedure

The quenching experiments were conducted with and without an electric field at atmospheric pressure conditions. First, DI water was subjected to vigorous nucleate boiling for degassing to avoid the influence of non-condensable gases. The degassed DI water was used for all the experiments. The coolant bath was filled with 2L of degassed DI water and heated up to saturation temperature. Simultaneously, the sample was heated inside the furnace to the desired temperature of 430 °C. The sample and bath temperatures were monitored using a data acquisition system. After reaching the desired temperature, the sample was immersed in the saturated DI water using an electronic slider. The temperature profile of the sample during

quenching was recorded using LabView, and simultaneously vapour layer/bubble behaviour was recorded using a high-speed camera. The data logging was done until the sample reached the thermal equilibrium with the coolant, marking the end of quenching experiments.

The same procedure was adopted for electric field assisted quenching experiments; however, before immersing the sample in DI water, the electric field was applied between the sample (anode) and counter electrode (cathode). During these experimentations, the applied voltage was varied from 0 to 200 V with an interval of 50 V. Above mentioned procedure is for a single test run. A minimum of five tests run for each experimental condition with fresh samples were performed, and their average value was taken for data processing. To analyse the effect of electric field polarity on quenching, the sample was connected to the cathode, and the same procedure was repeated. Table 1 provides the summary of experimental conditions in the present study. In addition to 0-200 V, we also performed experiments at 400 V and 600 V, but higher voltages exhibit an adverse effect on the quenching, which will be discussed in detail in Section 3.

To investigate the effect of oxidation, samples were repeatedly quenched without any surface cleaning between the test runs. This process was repeated up to six times. This ensures the formation of a stable oxide layer which facilitates the investigation of the effect of in-situ sample oxidation on quenching with and without an electric field. The repeated quenching experiments were conducted for all considered voltages and polarity. Finally, data from the experiments were processed to deduce the heat flux and cooling rate.

Table 1. Test matrix.

Sample	**Coolant**	**Temperature (°C)**		**Surface condition of the sample**	**Polarity**	**Voltage (V)**
		Sample	Coolant			
Cylindrical SS 316L	DI water	430 (initial)	100	Polished/ Repeatedly quenched (in-situ oxidised)	Anode/ Cathode	0 50 100 150 200

3. Computational study – Inverse heat conduction analysis

We computed the unknown boundary heat flux at the sample surface using the knowledge of temperature data at selected interior point during quenching via serial inverse heat conduction

algorithm proposed in Ref. [43]. A finite element domain was modelled, and inverse heat conduction algorithm was solved using TmmFE Inverse Solver. The following section details the physical model and governing equations for computing the heat flux.

3.1 Physical model

A single unknown heat-flux boundary was assumed along the sample surface. Fig. 3a shows the computational domain and the boundary conditions. The computational domain is the axisymmetric 2D structure modelled in the cylindrical coordinate system. The domain represents the mid-section of the sample where the thermocouple was mounted. A similar model was also used by Kumar [44] to determine the boundary heat flux during the quenching process. The grid of solution domain is shown in Fig. 3b. The detailed discussion of grid study and selection is provided in Section 4.2. Boundary S_1 represents the unknown heat flux, the heat transfer at S_2 is negligible considering the length of the sample, so it is neglected. Boundary S_3 along the axis of symmetry is assumed at adiabatic condition, $q'' = 0$. Table 2 shows the boundary conditions for inverse heat conduction model.

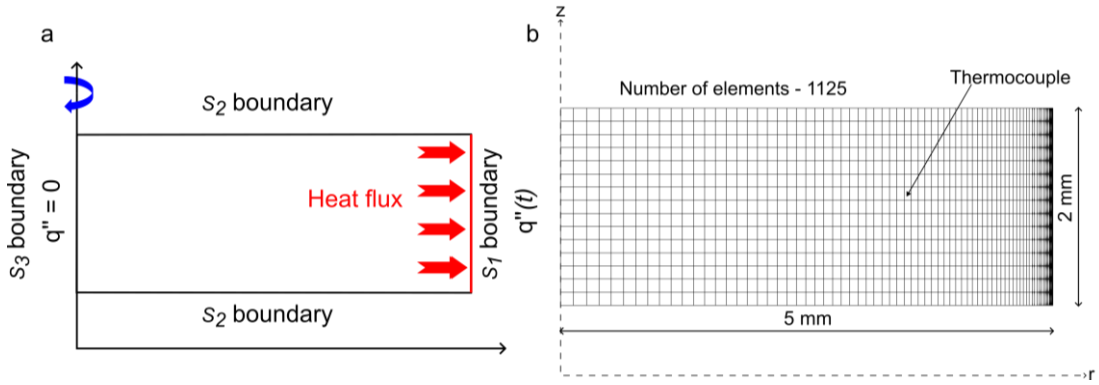

Fig. 3. (a) Computational domain. (b) Grid of solution domain.

Table 2. Boundary conditions for inverse heat transfer model.

Boundary surface	Boundary condition
S_1	$q(t) = -k\left(\frac{\partial T}{\partial r}n_r + \frac{\partial T}{\partial z}n_z\right), T(r,z,t) = T_{meas}(t)$
S_2	$q(t) = -k\left(\frac{\partial T}{\partial r}n_r + \frac{\partial T}{\partial z}n_z\right) = 0$
S_3	$q(t) = 0$ (adiabatic)

3.2 Governing equations

The equation that governs the transient heat conduction within the 2D computational domain in the cylindrical coordinate system is given as,

$$\frac{\partial}{\partial \mathrm{r}}\frac{k}{r}\left(r\frac{\partial T(r,z,t)}{\partial \mathrm{r}}\right)+\frac{\partial}{\partial \mathrm{z}}\left(k\frac{\partial T(r,z,t)}{\partial \mathrm{z}}\right)=\rho c_p\frac{\partial T(r,z,t)}{\partial t} \quad (1)$$

where k, ρ, and c_p are the thermal conductivity, density and specific heat capacity of SS 316L. To solve the serial inverse heat conduction model for heat flux during quenching the initial and boundary conditions are defined as follows,

Initial condition:

$$T_{(r,z,t)} = T_{initial} \quad (2)$$

at $t = 0$ where $T_{initial}$ = 430 °C

Boundary conditions:

$$-k\left(\frac{\partial T}{\partial r}n_r+\frac{\partial T}{\partial z}n_z\right) = q(t) \text{ on } S_1 \quad (3)$$

$$-k\left(\frac{\partial T}{\partial r}n_r+\frac{\partial T}{\partial z}n_z\right) = 0 \text{ on } S_2, \text{ and } S_3 \quad (4)$$

$$T(r,z,t) = T_{meas}(t) \quad \text{at } r = r_0; \quad (5)$$

$$t = 0 < t \leq t_{end} \quad (6)$$

where $T_{initial}$ is the initial temperature of the sample after its complete immersion into the coolant, $q(t)$ is the unknown heat flux quantity, $T_{meas}(t)$ is the time-dependent temperature data and r_0 is the radius of the sample. The algorithm for inverse heat conduction analysis is shown in Fig. 4.

To deduce the unknown heat flux, the objective function with respect to q is defined as follows,

$$J(q_m) = \sum_{i=1}^{r}\left(Y_{j,m+i-1} - \hat{T}^{+}_{j,m+i-1}\right)^2 \quad (7)$$

$J(q_m)$ is the linear least square norm, which is the sum of squared error between the measured and computed temperature at the measuring point inside the sample. This optimization is performed to minimize the difference between the measured and computed temperatures in future time steps. Here, $Y_{j,m+i-1}$ is the measured temperature, $\hat{T}^{+}_{j,m+i-1}$ is the computed temperature, j is the number of temperature sensors in the sample (j =1 in the current investigation), m is global time steps, i is the current time step and r is the total number of future time steps ($r = 4$, is considered in the present investigation).

For initialization of the numerical solver an arbitrary value for q_m is assumed and then heat conduction equation is solved for r future time steps. The optimization of $J(q)$ for q_m yields the correction term for deducing heat flux in $m+i$ time step is given as

$$(\Delta q)_m^k = \frac{\sum_{i=1}^{r} \left[Y_{m+i-1} - \hat{T}_{m+i-1}\right] \phi_i^{k-1}}{\sum_{i=1}^{r} \left(\phi_i^{k-1}\right)^2} \tag{8}$$

where k is number of iterations, and ϕ_i^{k-1} is the sensitivity coefficient which is expressed as

$$\phi_i^{k-1} = \frac{T_{m+i}\left(q_m^{k-1}(1+\epsilon)\right) - T_{m+i}\left(q_m^{k-1}\right)}{\epsilon q_m^{k-1}} \tag{9}$$

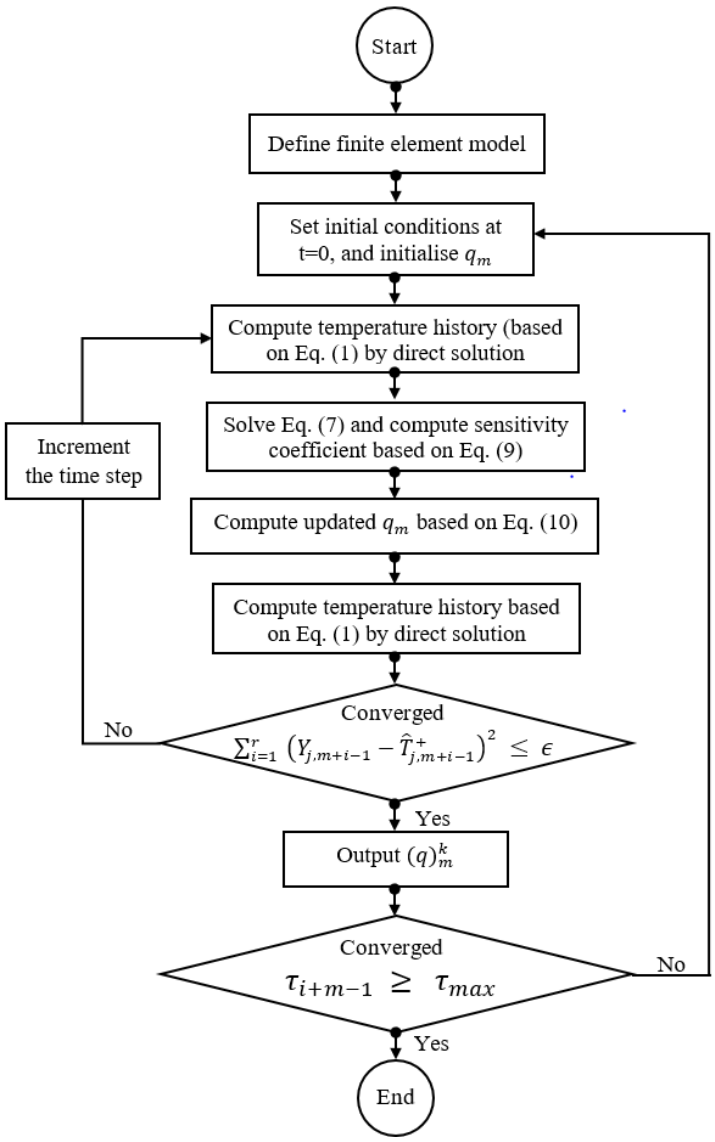

Fig. 4. Algorithm for inverse heat conduction analysis

The sensitivity coefficient signifies the variation in computed temperature for a slight change (ϵ) in $(q)_m$. Then this correction term is added to the heat flux obtained,

$$q_m^k = (q)_m^{k-1} + \frac{\sum_{i=1}^{r} [Y_{m+i-1} - \hat{T}_{m+i-1}]\, \phi_i^{k-1}}{\sum_{i=1}^{r} \left(\phi_i^{k-1}\right)^2} \tag{10}$$

This iteration procedure continues until the error between the measured and computed temperature minimize to the satisfies criterion,

$$\sum_{i=1}^{r} \left(Y_{j,m+i-1} - \hat{T}_{j,m+i-1}^{+}\right)^2 \leq \epsilon \tag{11}$$

where $\epsilon = 10^{-6}$. Once this condition is satisfied the iteration is stopped for time step τ_i and go to next time step τ_{i+1}. Then the obtained final iterative heat flux value is considered as the initial known heat flux value for next time steps. The loop ends when time $t = t_{end}$.

3.4 Uncertainty analysis

This section provides the uncertainties in the derived parameters, such as heat flux and cooling rate. The heat flux was computed using inverse heat conduction analysis (explained in Section 3), and the cooling rate was determined based on the method of computing the time derivative of the sample temperature ($T_{(r,t)}$) throughout the quenching process [45,46]. The uncertainties in the computed parameters are determined based on the uncertainty analysis method developed by Blackwell and Beck [47]. For, instance, heat flux estimated via inverse heat conduction analysis includes the individual uncertainties in the parameters used and this relation is given as,

$$\delta q^c = \sqrt{\sum_{i=1}^{n} \left(\frac{\partial q^c}{\partial x_i}\, \delta x_i\right)^2} \tag{12}$$

$$= \sqrt{\left[\frac{\partial q^c}{\partial \Delta T^m}\, \delta \Delta T^m\right]^2 + \left(\frac{\partial q^c}{\partial k}\, \delta k\right)^2 + \left(\frac{\partial q^c}{\partial C_p}\, \delta C\right)^2} \tag{13}$$

where ΔT^m, k and $C = \rho c_p$ are the parameters used for computing the heat flux. Table 3 summarizes the maximum uncertainty in heat flux and cooling rate. the experimental uncertainties. The maximum uncertainty in thermocouple measurement is 0.1% and the position uncertainty is 2.5%.

Table 3. Summary of uncertainties in derived parameters.

Parameter	Uncertainty (max)
Heat flux	13.5%
Cooling rate	7.2%

4. Results and discussion

The research hypothesis is that hydrogen-rich vapour layer/bubbles improve liquid circulation at the sample surface and enhance the quenching heat transfer. To test this hypothesis, we performed immersion quenching of SS316L in DI water at saturated conditions under atmospheric pressure with and without an electric field. Then the cooling profile of the sample, heat flux variations, vapour film behaviour, and cooling surface characteristics are analysed in detail. It is worth mentioning that the selected initial temperature of the sample (430 °C) and DI water at saturation temperature reflects the thermal crisis situation in high-energy density systems and ensure sufficient film boiling duration to analyse the effect of the electric field in detail.

4.1 Analysis of the experimental cooling curve of SS 316L sample

Fig. 5 shows the cooling curve of SS316L in DI water at saturated conditions with the demarcation of the transient boiling heat transfer regimes along with their corresponding vapour film/bubble behaviour. As the sample cools from the initial temperature of 430 °C, the cooling curve shows the prominent transient boiling heat transfer regimes: film, transition, and nucleate boiling. When the sample at a temperature of 430 °C is plunged into saturated DI water due to its high superheat, the liquid in its vicinity will instantly evaporate and form a stable vapour film around the sample, which cuts off the direct solid-liquid contact. This boiling phenomenon is called film boiling. In film boiling, the sample cools mainly by radiation and convective heat transfer through a stable vapour layer.

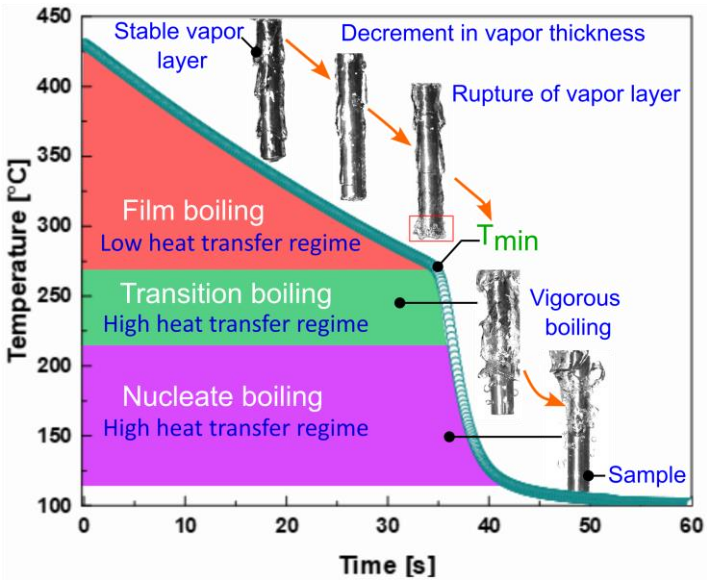

Fig. 5. Cooling curve of SS316L in DI water at saturated condition.

The visualization studies show that the oscillation of the liquid-vapour interface leads to a reduction in vapour layer thickness with respect to time. The periodic oscillation of the liquid-vapour interface is due to vapour growth and its buoyancy-driven motion in the vapour layer along the sample. As the sample temperature gradually decreases over time, the vapour layer becomes thinner and starts to collapse. Usually, in quenching at saturated conditions without any external modification, the vapour layer starts to collapse at the bottom end of the sample and propagates toward the top end. The temperature at which the vapour film collapse is known as T_{min}. Once the vapour layer breaks (or below T_{min}), the sample enters the transition and nucleate boiling regime.

Transition and nucleate boiling facilitate the rapid heat removal from the sample due to vigorous bubble nucleation, growth, and departure. After the vapour film collapses, the rewetting of the sample happens. The rewetting leads to the occurrence of violet boiling at the sample surface. The numerous nucleation sites become activated, and vapour bubbles start to emanate from the surface, which inevitably coalesce to form vapour chunks before departing. Such vigorous boiling enables the rapid cooling of the sample. Therefore, the cooling curve shows a sharp drop in temperature at transition and nucleate boiling regime. The observed phenomena are in agreement with the previous literature [39].

However, a rapid heat transfer rate is observed in transition boiling until Critical Heat Flux (CHF) and fully developed nucleate. It is worth mentioning that in transient boiling or quenching, CHF indicates that the sample experienced intense transition boiling, and the heat transfer rate builds up to reach the peak heat extraction rate from the sample during quenching. After CHF, the heat transfer rate comes down with the sample temperature. Finally, the cooling curve displays the flat plateau as it approaches the saturation temperature of the liquid due to the single-phase convective heat transfer.

From the above discussion, we can infer that there are two important aspects of the cooling curve: (a) time taken to reach T_{min}, and (b) time taken to reach maximum heat flux or CHF. Here, we determined the T_{min} using the standard definition in the literature [48]. Boundary heat flux was calculated by solving the inverse heat conduction problem, as explained in Section 3.

4.2 Validation of inverse heat transfer model

The described inverse algorithm provides the unknown boundary heat flux during quenching. The estimated temperature is compared with experimental data for model validation and to determine the optimum grid size and time step for calculating the boundary heat flux.

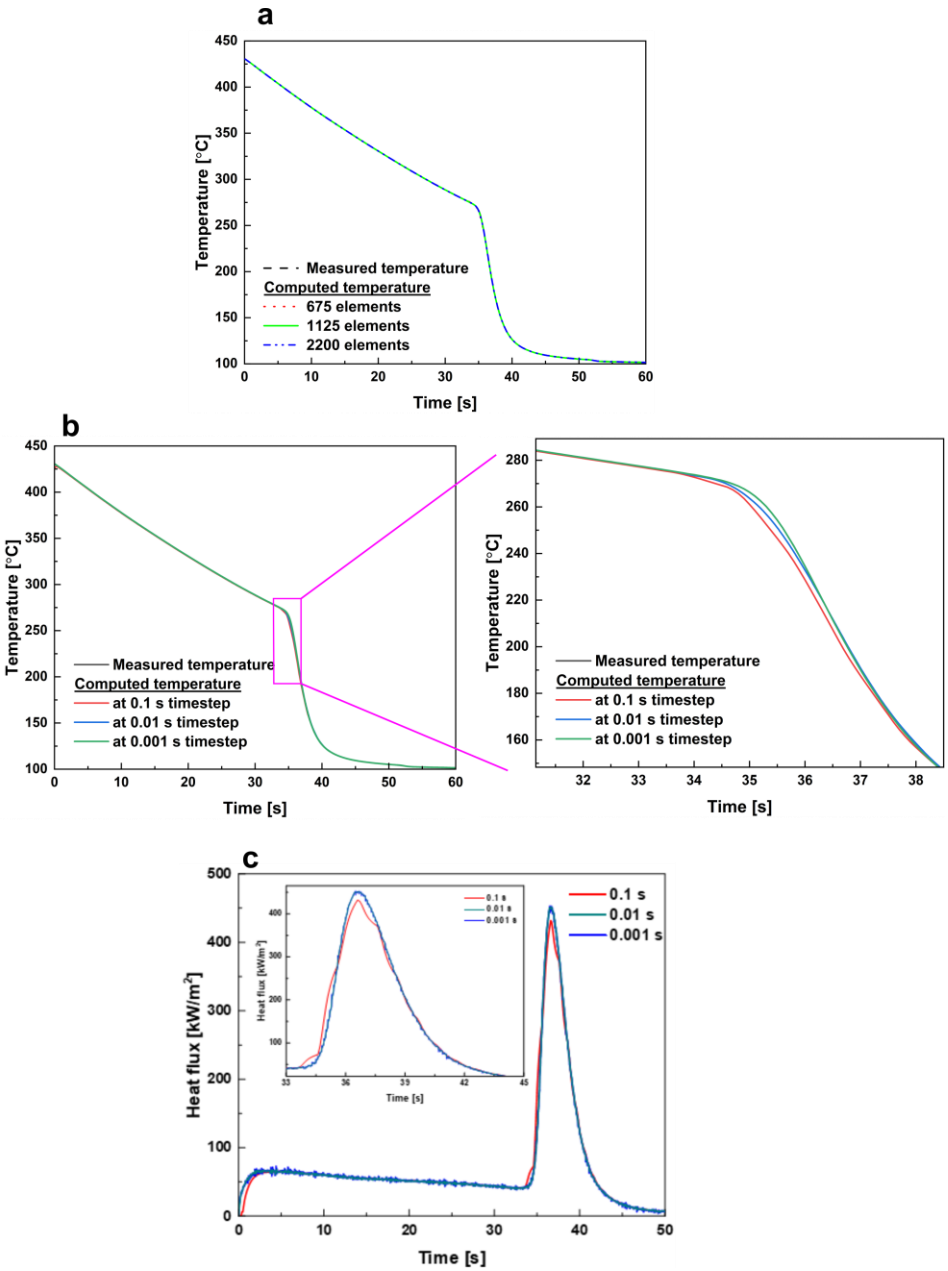

Fig. 6. (a) Comparison of experimental temperature data with the estimated temperature at different grid components, (b) comparison of experimental temperature data with the estimated temperature at different time steps, and (c) comparison of boundary heat flux calculated at different time steps.

The computational domain was simulated using different grid sizes with an intense distribution of elements at the boundary, as mentioned in Section 3.1. Fig. 6a compares the estimated temperature at different grid components with the experimental temperature data. There is no significant deviation between the measured and estimated data. The estimated temperature closely matches the experimental temperature, showcasing the inverse algorithm's accuracy and

reliability. The negligible influence of grid size on the inverse solution is also reported in Ref. [49]. Hence, the simulations were performed with 1125 grid elements (see Fig. 3b).

Further, the influence of the time step on estimated temperature was simulated, and the obtained results show a slight variation in transition and nucleate boiling regime, as displayed in Fig. 6b. At 0.1 s, there is a slight deviation in estimated temperature from the measured temperature, especially when the boiling mode shift from film to transition and transition to nucleate. However, this deviation comes down with the increase in the time step. At 0.01 s and 0.001 s time steps, the deviation between the experimental and estimated temperature is minimal.

The calculated boundary heat flux in Fig. 6c indicates that the heat flux curve matches 0.01 s and 0.001 s. The heat flux curve of 0.1 s time step shows the chaotic nature in the high heat transfer regimes, and there is an appreciable difference from the heat flux curve of 0.01 s. As the time step increases from 0.01 s to 0.001 s, the heat flux curve matches and exhibits a similar nature with a smooth transition at high heat transfer regimes. We calculated the heat flux at 0.01 s to minimize the computational load. The same model and simulation statistics were successfully incorporated for calculating boundary heat flux in the presence of an external electric field.

4.3 Enhancement effects of electric field on quenching and heat flux characteristics

This section discusses the influence of the applied electric field and electrode polarity on the conventional cooling curve of SS 316L. Fig. 7a and 7b illustrate the cooling curves of the SS 316L sample as anode and cathode at different voltages ranging from 0 to 200 V at the interval of 50 V. The cooling curve mentioned as 0 V illustrates the cooling profile of SS 316L sample quenched without an external electric field, which is taken as a reference for comparison. In the presence of an electric field, the cooling curve exhibits similar nature, such as film boiling followed by transition and nucleate boiling, as that of a conventional cooling curve.

It is evident that the applied electric field accelerates the quenching for both electrode polarities. In Fig. 7a and 7b, the cooling curves of the electric field assisted quenching shift towards the left (smaller time frame), indicating faster cooling than the quenching without an electric field (0 V). When the sample acts as an anode/cathode, the film boiling duration comes down with increased applied voltage, so the sample enters the transition and nucleate boiling much faster than quenching without an electric field in the presence of applied voltage. Even though the quenching enhancement increases with applied voltage, the enhancement rate comes down at higher voltages. Especially in the case of the sample as a cathode, it is evident from Fig. 7b that the cooling curves of 150 V and 200 V are closer. So, in the present study,

the maximum applied voltage is limited to 200 V. (For more details about the effect of higher voltages on T_{min}, refer Fig. S1, Supplementary reference).

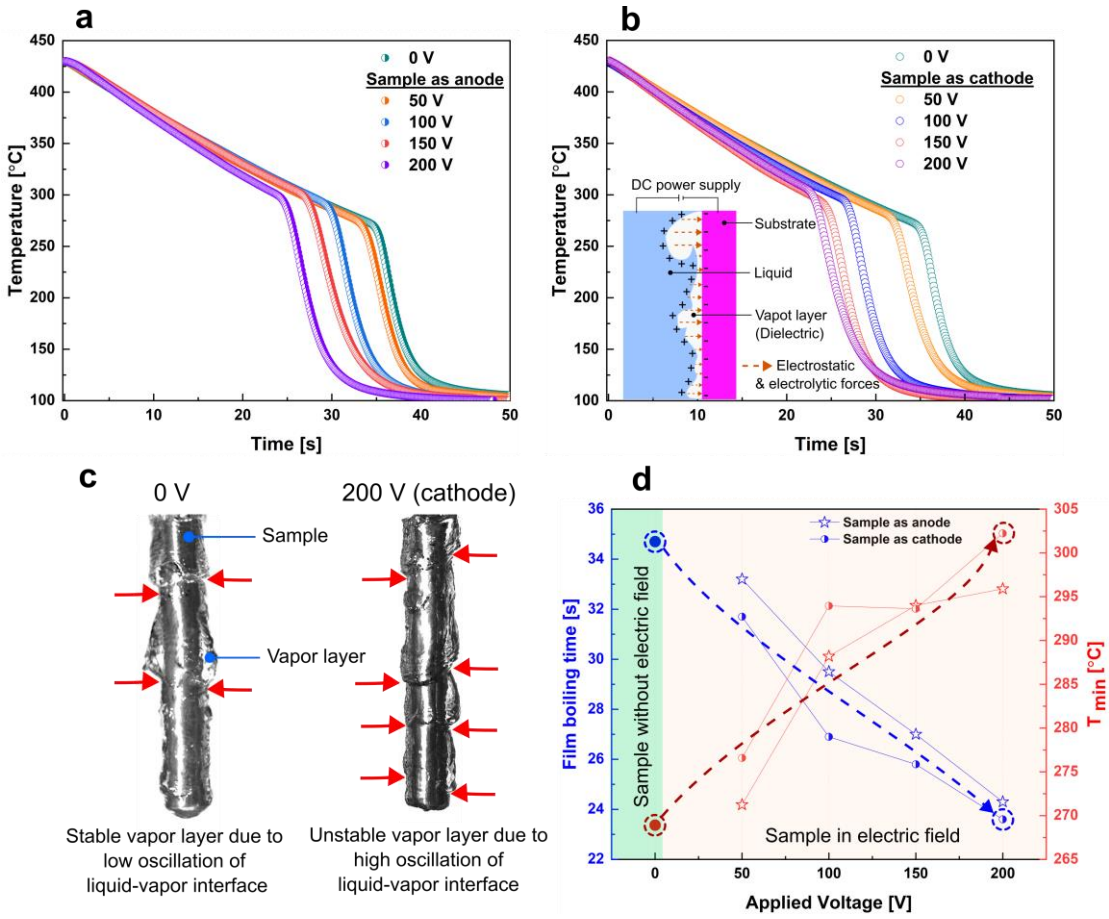

Fig. 7. (a) and (b) Comparison of the cooling curves of SS 316L sample as anode and cathode at different voltages ranging from 0 to 200 V at the interval of 50 V, (c) high-speed visualization of film boiling regime of polished sample (0 V) and cathode sample at 200 V, and (d) variation of film boiling time and T_{min} as a function of sample polarity at any given voltage.

At a potential of 200 V, the film boiling duration of the cathode sample reduces by 33% compared to without electric field conditions. This happens because the applied electric field increases the instabilities at the liquid-vapour interface by introducing the additional electrostatic and electrolytic force field. The subset figure in Fig. 7b illustrates the attraction of liquid film to the cathode surface. The electrostatic force tends to pull the water molecules toward the sample surface, it reduces the vapour layer thickness and enhances the film boiling heat transfer. Such effect is also reported in Ref. [36]. The developed electrostatic force, along with the convective shear force, disturbs the stability of the vapour layer.

This increases the pressure gradient, which causes the turbulent motion of the vapour-liquid interface. Fig. 7c represents the high-speed visualization of the film boiling regime of the

polished sample (0 V) and cathode sample at 200 V. The film boiling of a polished sample without an electric field exhibits a stable vapour layer with occasional oscillations. In contrast, the film boiling of a cathode sample with an electric field (at 200 V) exhibits chaotic vapour layer behaviour and frequent oscillations. Therefore, film boiling heat transfer increases in the presence of the electric field. Eventually, the vapour layer crumbles under the influence of the applied electric field, and consequently, T_{min} increases, and the sample cools faster. Such enhanced heat transfer is due to the combined action of electrostatic attraction and electrolytic activity at the sample surface. However, the enhancement observed in electric field assisted quenching varies significantly with electrode polarity.

4.3.1 Impact of electrode polarity

Fig. 7a and 7b show that at the beginning of quenching, for the initial 5 s, there is no appreciable difference in the cooling behaviour of the anode and cathode. The influence of applied electrode polarity becomes apparent as the sample superheat decreases or quenching progresses. Fig. 7d showcases the variation of film boiling time and T_{min} as a function of sample polarity at any given voltage. Overall, the cathode sample displays a higher quenching effectiveness than the sample as anode. When the sample act as a cathode for all applied voltages, except 150 V, the film boiling time reduces, and T_{min} increases compared to the sample as anode. Similarly, compared to the sample quenched without an electric field, T_{min} of cathode at 200 V increases from 268 °C to 301 °C. It indicates that other variables apart from electrostatic attraction play a role in quenching heat transfer enhancement.

The enhancement in quenching heat transfer varies with electrode polarity due to the self-ionization of saturated DI water that leads to the formation of hydronium (H_3O^+) and hydroxide ions (OH^-),

$$2H_2O \rightleftharpoons H_3O^+ + OH^- \tag{14}$$

According to Le Chatelier's principle, the temperature rise promotes the self-ionization of water. The concentration of OH^- and H_3O^+ will increase with water temperature due to molecular collision. The relationship between the equilibrium constant for the formation of OH^- and H_3O^+ and temperature is given by Vant Hoff equation,

$$ln\left(\frac{Kw_2}{Kw_1}\right) = \frac{\Delta H^\circ}{R}\left(\frac{1}{T_1} - \frac{1}{T_2}\right) \tag{15}$$

where ΔH° is the enthalpy change, R is the universal gas constant, Kw_1 and Kw_2 are equilibrium reaction constant at temperature T_1 and T_2. Thus, the formation of H_3O^+ and OH^- increases

with the rise in temperature of DI water. It is worth mentioning that a coolant bath is an open system at atmospheric pressure conditions. A strong affinity of saturated DI water towards CO_2 leads to the formation of hydrogen carbonate ions (HCO_3^-) by the following reactions,

$$CO_2 + H_2O \rightleftharpoons \mathrm{H}_2CO_3 \tag{16}$$

$$\mathrm{H}_2CO_3 \rightleftharpoons H^+ + HCO_3^- \tag{17}$$

These ionic species alter the electrolytic activity of DI water, which in turn manipulates the type of vapour/gaseous atmosphere prevailing at the surface of the sample. The reduction of water produces hydrogen at the cathode and oxygen at the anode. However, at higher superheat, SS 316L has a higher affinity towards hydrogen adsorption than oxygen because of hydrogen's low molecular weight and relatively smaller size [50].

During the film boiling of the cathode sample, the applied electric field pulls the water molecules toward the sample surface. This electrostatic attraction destabilizes the developed vapour layer and supports the sample-liquid contact. Then the water molecules spontaneously undergo electrolysis at the cathode sample, producing hydrogen. At the initial condition, some hydrogen produced will dissolve into bulk liquid [41], and some escape through the vapour layer and vent out at the top end of the sample. However, the hydrogen becomes supersaturated and trapped at the sample surface due to continuous electrolytic activity. Due to the hydrogen adsorption and evolution at the cathode surface, the liquid-vapour interface undergoes a series of pulsations. Ultimately the vapour layer thickness reduces and leads to its early rupture. This results in better heat extraction from the cathode sample than the anode sample. Hence the cooling performance at the cathode is better than that at the anode.

4.3.2 Heat flux and cooling rate characteristics

Fig. 8a and 8b show the variation of heat flux with time for samples as anode and cathode compared to samples without electric field.

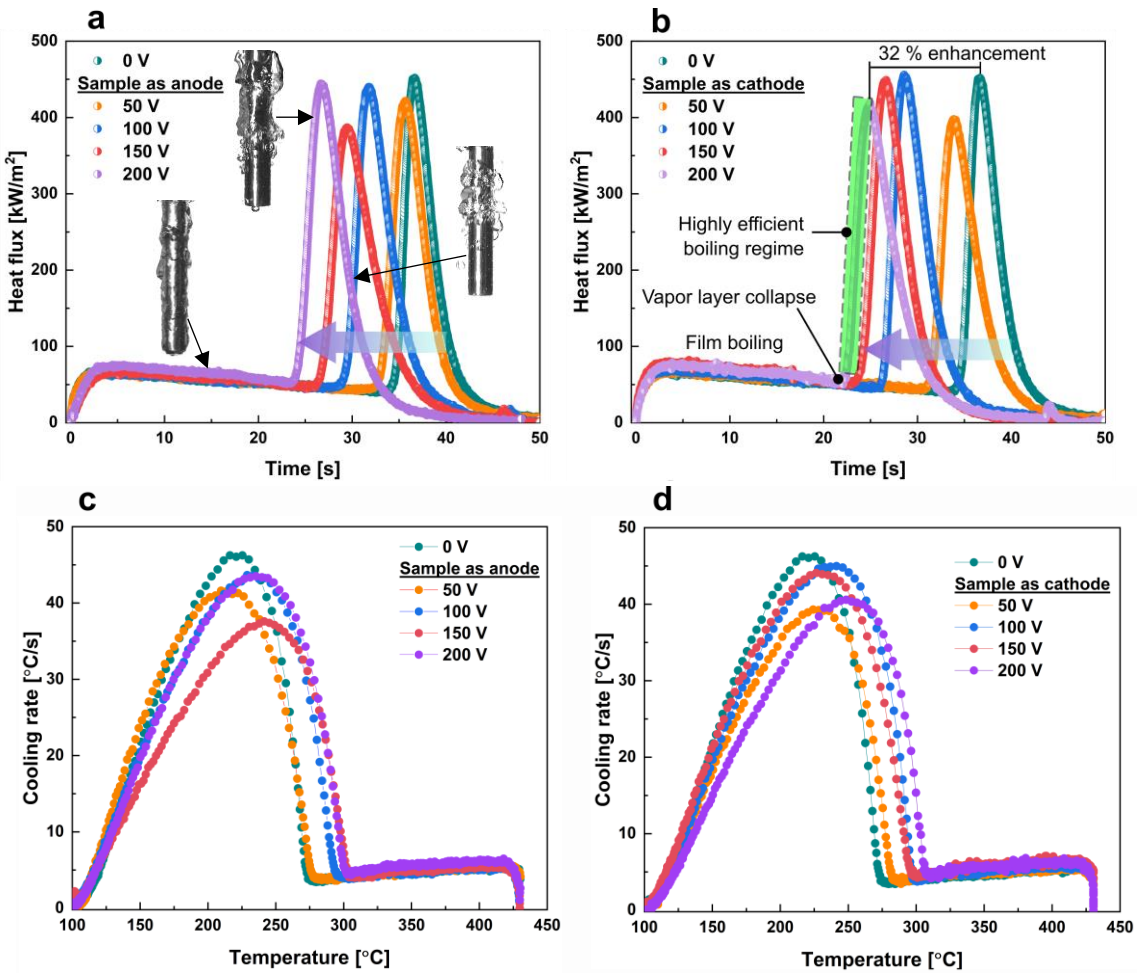

Fig. 8. (a) and (b) Comparison of the heat flux characteristics of the sample without an electric field with the sample as anode and cathode at considered voltages. (c) and (d) Comparison of the cooling rate characteristics of the sample without electric field with the sample as anode and cathode at considered voltages.

The computed heat fluxes agree with the experimental results of high-speed visualisation of vapour/bubble behaviour in presence of electric field, as shown in Fig. 8a. The heat flux curves of both the anode and cathode shift leftwards for all applied voltages, with the cathode at a DC potential of 200 V displays the maximum shift. In the presence of an electric field, the sample reaches the maximum heat flux much faster than the sample without an electric field.

It is worth mentioning that heat flux curves exhibit a similar nature for quenching with and without an electric field. At the beginning of quenching, the heat flux curve shows a slight increase in the heat flux, followed by a decreasing flat plateau. This region indicates the film boiling, as shown in Fig. 8a. As discussed earlier, the stable vapour layer hinders the heat transfer rate, which causes the slow cooling of the sample at high-temperature regimes. However, the applied electric field reduces the vapour layer thickness and increases the heat transfer rate in film boiling.

From Fig. 8a and 8b, it is evident that there is a sharp increase in heat transfer when the sample enters the transition boiling regime. The highlighted portion in Fig. 8b indicates the highly efficient transition boiling regime in the quenching process. Here the sample undergoes intense boiling, which extracts the majority of heat from the sample within the span of a few seconds (for a cathode sample at a DC potential of 200 V, the time span is 2.8 s). The transition boiling ends with CHF, and then nucleate boiling occurs. For the cathode sample at 200 V CHF occurs 39% faster than the sample without an electric field. Here, achieving CHF faster in the cooling curve signifies that the sample enters the effective heat transfer regime more quickly, and as a result, the sample cools down at a faster rate. Although the heat flux range in nucleate boiling is similar to transition boiling, the curve exhibits a negative slope, which asymptotically approaches the low heat transfer rate. To get further insight, we analyse the cooling rate variation concerning sample temperature for all the samples considered in this investigation.

Fig. 8c and 8d show the variation of cooling rate for the sample as anode and cathode in comparison with the sample without an electric field. We can infer from Fig. 8c and 8d that when the electric field is applied, there is an upward shift (high temperature) in the curve. The maximum variations in cooling rate occur on a particular temperature range corresponding to transition and fully developed nucleate boiling. The maximum cooling rate variations for the sample without electric field, sample as anode and cathode at 200 V occurs at 274 °C to 216 °C, 300 °C to 252 °C and 310 °C to 265 °C, respectively. It reflects that the applied electric field increases the transition and nucleate boiling heat transfer. Among the samples as cathode and anode, the cathode exhibits better heat transfer performance, and such effect is due to the more nucleation site developed by hydrogen molecules at the sample surface. Interestingly, heat flux and cooling rate analysis also reveal a slight decrease in CHF and peak cooling rate even though T_{min} increases in the presence of the electric field. This is mainly due to the in-situ surface oxidation during the quenching process. So, we performed consecutive quenching experiments to study the effect of in-situ surface oxidation on the cooling profile of the sample with and without an electric field.

4.4 Effect of in-situ oxidation on quenching characteristics

This section details the influence of in-situ surface oxidation, under an applied electric field, on quenching heat transfer using the cooling curve, heat flux analysis, and high-speed visualizations. To study the effect of oxidation on quenching heat transfer, we followed the method adopted by Kim et al. [51], where the sample was quenched repeatedly without any surface cleaning in-between. Fig. 9(a-c) shows the cooling curves, and Fig. 9(d-f) shows the heat flux characteristics of the SS316L sample quenched repeatedly (up to six test runs) without

and with an electric field at different polarities. The repeated quenching experiments were performed only at 200 V because the quenching performance of the anode/cathode at 200 V was found to outperform the other applied voltages.

Fig. 9a displays the cooling curves of six consecutive quenching sample test runs without an electric field. It is evident that the in-situ oxidation did not influence the T_{min}. The cooling curves of the repeated quenching test show that the data are within the scattering range without any striking deviations. On the other hand, the first and second tests have minimal variations in transition and nucleate boiling regimes, but this variation comes down at higher test runs, as shown in the subset graph of Fig. 9a. The cooling curves overlapped after the third test run and demonstrated similar performance. This is due to the stabilization oxide layer during quenching. The observed results are in agreement with the previous studies [38,39].

Similar performance is also exhibited by the repeatedly quenched anode sample at 200 V. Fig. 9b shows that cooling curves show marginal variation in the T_{min} of the first and sixth test run with the film boiling duration decreased by 5.3%. However, the cooling curves exhibited similar performance from the third to the sixth test run without any further enhancement. The combined effect of oxidation and electric field slightly shifts the heat transfer curves towards the left, which indicates that T_{min} occurs early with in-situ oxidation. The metal oxides formed on the surface possesses a lower heat capacity (ρc_p) compared to the bulk metal [52]. It results in a temporal drop in wall temperature, which increases the vapour layer instabilities and enhances the film boiling heat transfer.

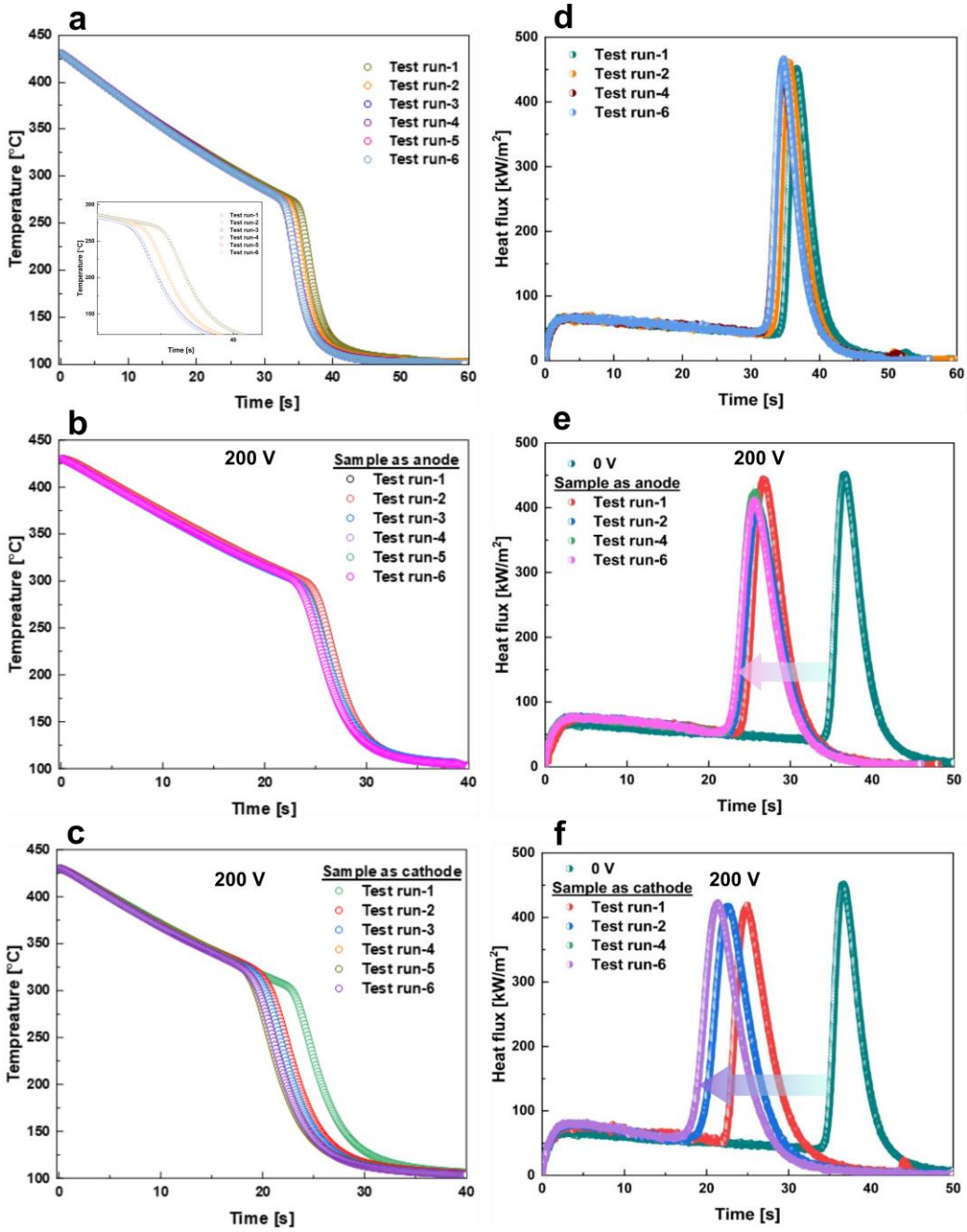

Fig. 9. (a-c) Comparison of the cooling curves, and (d-f) comparison of the heat flux characteristics of SS316L sample quenched repeatedly (up to six test runs) without and with the electric field at different polarity (200 V).

Interestingly, T_{min} is more vulnerable to in-situ surface oxidation if the sample act as a cathode at 200 V. The presence of hydrogen has a significant effect on altering the quenching performance. Fig. 9c shows a significant difference between the first and sixth test runs, where the film boiling duration decreased by 22%. These results highlight the rapid heat transfer. However, after the fourth run, this enhancement almost becomes stable and further quenching does not improve the heat transfer rate.

The heat flux curves, Fig. 9(d-f), show the CHF and heat transfer variations. As expected, the heat flux curves of the sample (0 V) shown in Fig. 9d also illustrate no appreciable difference in T_{min} and CHF. The heat flux curves of sample anode a1 200 V, Fig. 9e showcase that the heat transfer in transition and nucleate boiling slight deviations in the initial test runs but becomes constant after the third test run. The marginal decrement in CHF occurs due to excessive oxidation in the presence of an applied electric field. In the case of the sample as a cathode at 200 V, Fig. 9f displays no significant change in the CHF of successive test runs, but CHF keeps shifting leftwards until the fourth test run and remains stable up to the sixth test run. Fig. 10(a-c) illustrates the variations in the occurrence of peak cooling rates respective to test runs of different sample conditions. As expected, the peak cooling rate occurs much early for the sample as the cathode, which is followed by the anode. Overall, the in-situ oxidised cathode sample at 200 V exhibits a 55% reduction in film boiling duration, and T_{min} increased from 268 °C to 322 °C compared to the bare sample (0 V), see Fig. 10d. The following section explains the primary reason for enhancement in quenching heat transfer characteristics due to repeated quenching.

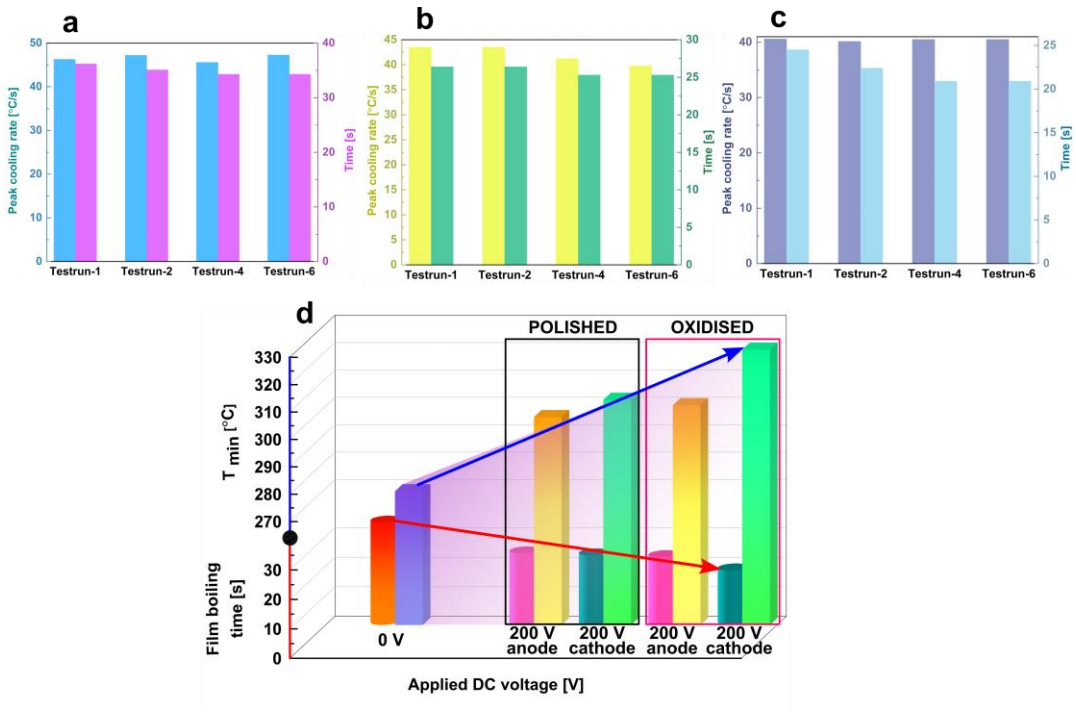

Fig. 10. Variation in the occurrence of peak cooling rate with respective to test run of different sample conditions: (a) 0 V, (b) anode at 200 V, (c) cathode at 200 V, and (d) variation of film boiling time and T_{min} as a function of sample polarity and surface conditions at 200 V.

4.4.1 Mechanism governing the quenching heat transfer enhancement

Fig. 11 represents the high-speed visualization of film boiling regimes of the repeatedly quenched sample without an electric field (0 V) and the sample as a cathode at 200 V for the first and sixth test runs. Repeatedly quenched cathode sample shows remarkable variations in vapour layer behaviour, while the sample without an electric field shows negligible variations.

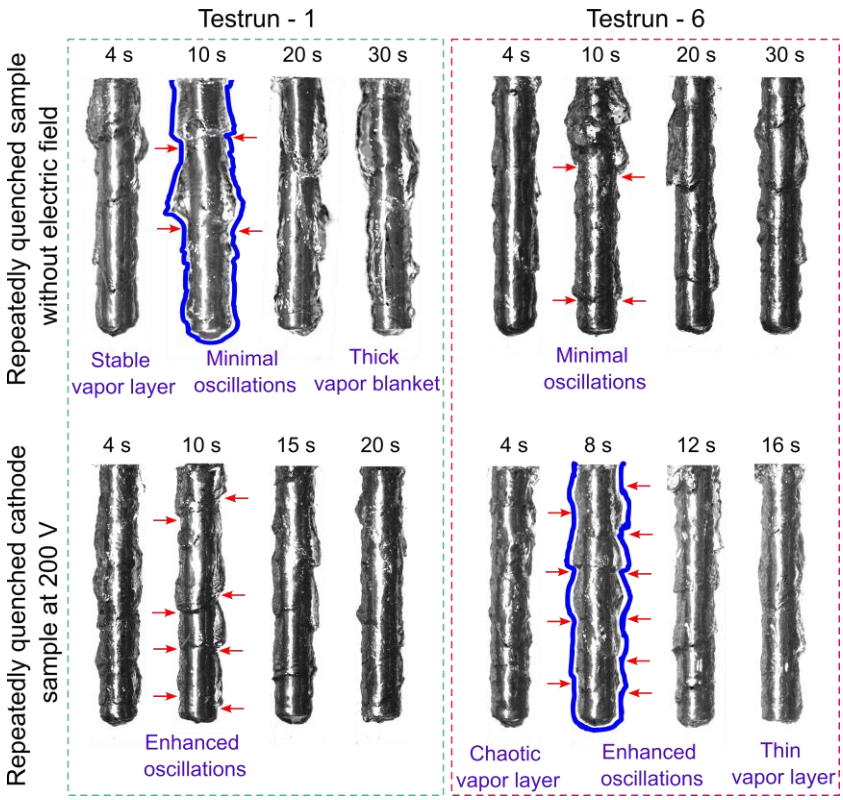

Fig. 11. High-speed visualization of film boiling regimes of the repeatedly quenched sample without electric field (0 V) and sample as a cathode at 200 V for the first and sixth test runs.

In the case of the sample without an electric field, the film boiling in the first test run exhibits a stable, thick vapour layer with minimal oscillations. The vapour layer behaviour and heat transfer performance are almost similar and constant even though the sample was subjected to repeated quenching. It is due to the formation of a stable oxide layer over the SS316L sample. The negligible influence of the oxide layer on film boiling in repeated quenching experiments agrees with [39]. For the cathode sample at 200 V, with an increase in the test run, the vapour layer exhibits chaotic nature with a series of oscillations. This indicates the local collapse of the vapour layer at several places (red arrow markers in Fig. 11) along the sample surface. The primary reason behind such chaotic nature of the liquid-vapour interface is due to surface discontinuities such as the formation of surface cavities and the hydrogen evolution and its adsorption in the oxide layer. Fig. 12 illustrates the physical mechanism governing the film boiling heat transfer

enhancement of repeatedly quenched cathode samples at 200 V. In the presence of an electric field, the electrochemical reaction between the cathode sample (mostly Fe, Cr) and water molecules leads to the formation of the oxide layer with surface imperfections. The surface imperfections, e.g., microcavities, lead to a discontinuous vapour layer, as shown in Fig. 12a. Fig. 12b shows the enhanced boiling at the microcavity in the oxide layer. The microcavities ensure direct contact between the sample and liquid, which enhances the liquid replenishment of the sample even at higher superheat. Then due to electrolytic activity, the hydrogen molecules are produced at the micro-cavity. The entrapped hydrogen increases the nucleation and facilitates the formation of numerous vapour bubbles. As a result, film boiling heat transfer increases. To this extent, the formed oxide layer was analysed using SEM, XRD, and EDS.

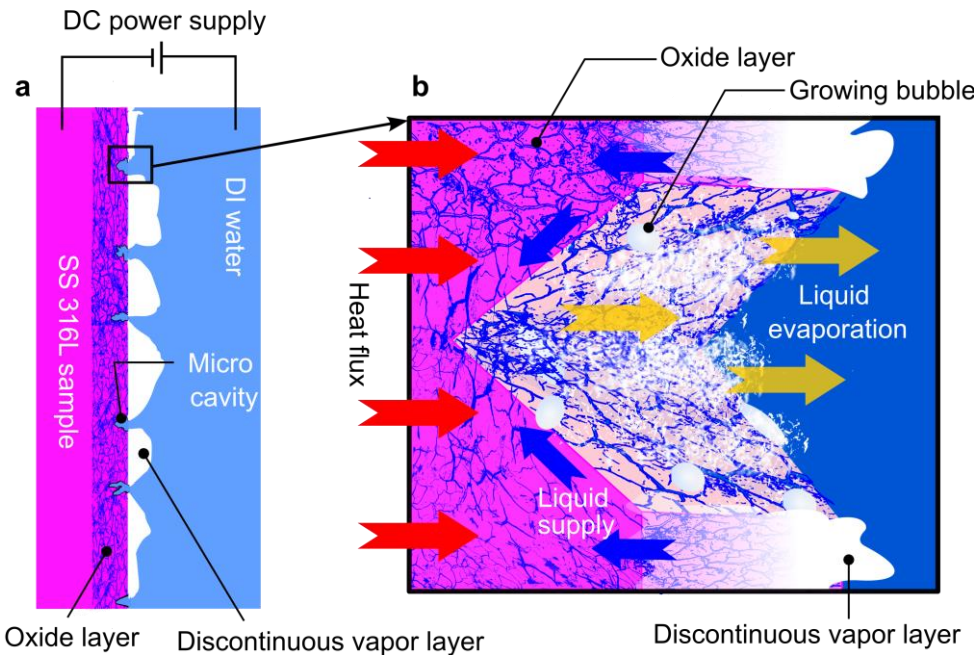

Fig. 12. Illustration of the physical mechanism governing the film boiling heat transfer enhancement in repeatedly quenched cathode sample at 200 V: (a) discontinuous vapour layer, and (b) enhanced boiling at the microcavity in the oxide layer.

The SEM images in Fig. 13 detail the variation of surface morphology for the bare sample and repeatedly quenched samples (sixth test run): at 0 V, anode sample at 200 V, and cathode sample at 200 V. Fig. 13a shows the surface morphology of bare sample. The repeatedly quenched sample without an electric field shows textured oxide layer formation without cavities or grooves, as in Fig. 13b. The anode sample (Fig. 13c) shows the particulate oxides and thick textures of oxide layer formation with grooves. It confirms that repeatedly quenched anode sample at 200 V undergoes enhanced oxidation. Therefore, more nucleation sites are developed, which causes the leftward shift of the cooling curve compared to 0 V. Repeatedly quenched cathode sample at 200

V, see Fig. 13d, shows the deposition of nanoscale metal oxide particles (avg. size = 320 ± 0.09 nm) and microcavities (avg. size = 1.6 ± 0.75 μm). The formed nano-oxide particles increase the surface area, and cavities promote bubble nucleation via hydrogen entrapment. Such developments on the boiling surface remarkably enhance the quench heat transfer.

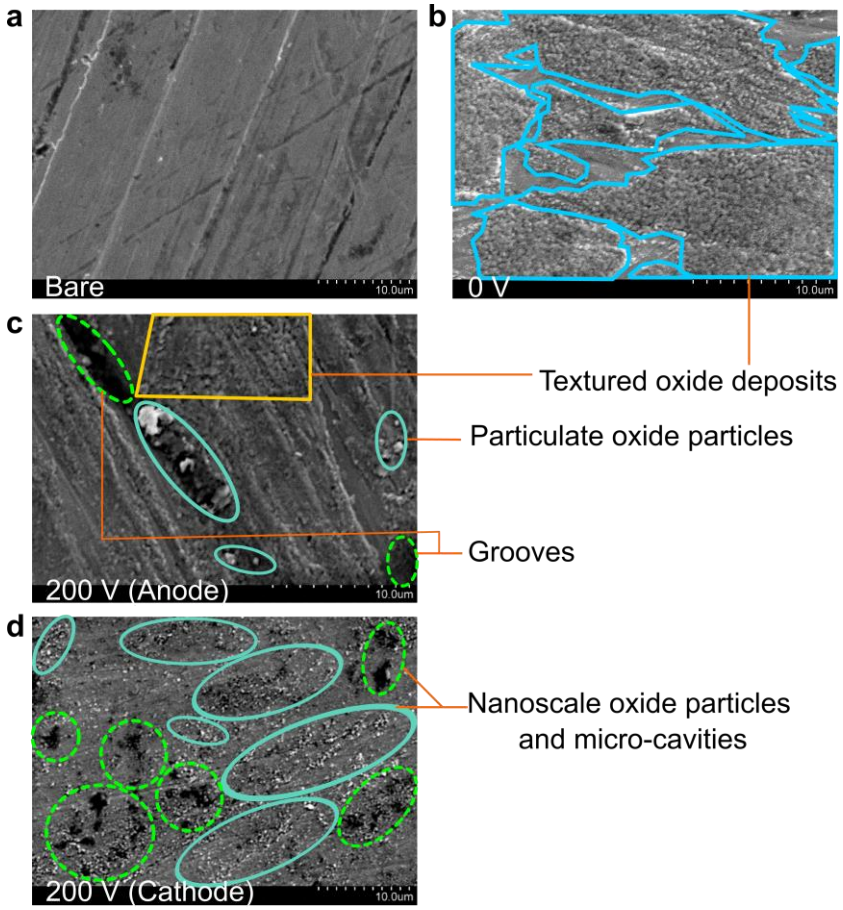

Fig. 13. SEM images of: (a) bare sample, repeatedly quenched samples (sixth run), (b) at 0 V, (c) anode sample at 200 V, and (d) cathode sample at 200 V.

In addition, XRD analysis of the repeatedly quenched cathode sample at 200 V display the peak broadening and shifting towards the higher angle. Fig. 14 compares the XRD patterns of the bare sample and repeatedly quenched samples (sixth run) without and with an electric field (cathode sample at 200 V). The peak shifts to a lower angle than the bare sample in the repeatedly quenched sample without an electric field. This is due to the increase in crystallite size. On the other hand, compared to the bare sample, the XRD patterns of repeatedly quenched cathode samples show the peak shifts to a higher angle and peak broadens. It is due to lattice strain and small crystallite size. Table 4 provides the details of the micro-strain. Further, the variation in the intensity also highlights the grain refinement of oxides particles. This confirms

the formation of nanoscale crystallites on the boiling surface, which enhances the surface area and favours rapid quenching heat transfer.

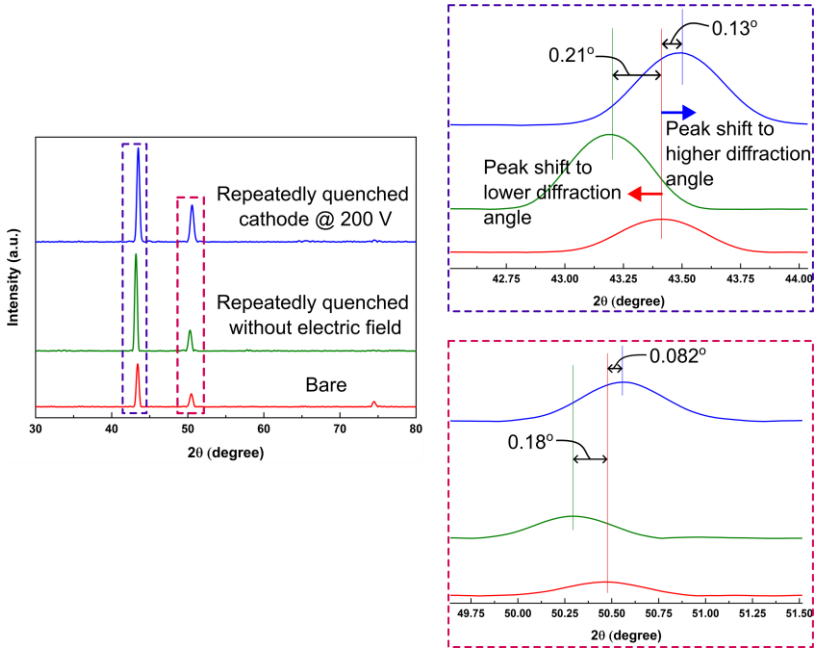

Fig. 14. Comparison of the XRD patterns of bare sample and repeatedly quenched samples (sixth run) without and with an electric field (cathode sample at 200 V).

Table 4. Micro-strain calculated from XRD data.

Sample	**Micro-strain (× 10^{-3})**
Repeatedly quenched without an electric field	2.09
Repeatedly quenched anode at 200 V	3.52
Repeatedly quenched cathode at 200 V	5.88

It is also evident from SEM and XRD analysis that in-situ oxidation and oxide depositions [Fe_3O_4, $FeCr_2O_4$, and Fe_2O_3] are very distinct in an electric field. EDS analysis, Fig. 15, reveals that repeatedly quenched cathode sample at 200 V exhibits selective in-situ oxidation compared to other samples. The selective in-situ oxidation happens at the cathode because the reduction reaction and entrapment of hydrogen bubbles prevent the oxide scale formation at the sample surface.

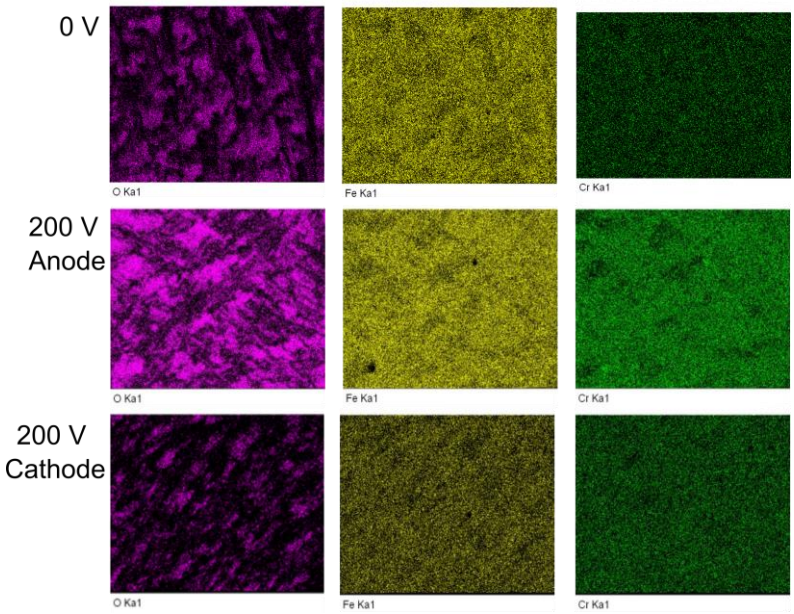

Fig. 15. EDS analysis of repeatedly quenched samples (6th run) at 0 V, anode and cathode at 200 V.

In the case of sample as a cathode, the entrapped hydrogen reduces the activation energy for bubble nucleation and improves the bubble density via liquid pumping. Further, the evolution of trapped hydrogen bubbles from the oxide layer creates the suction pressure, which pumps the liquid to the nucleation site and increases the bubble density. Fig. 16 shows enhanced transition and nucleate boiling at the surface of the repeatedly quenched cathode sample at 200 V. The magnified image in Fig. 16 shows micro-droplets at the previously formed bubble. This confirms that hydrogen bubbles via liquid pumping promote heterogeneous nucleation and increase the bubble density, thereby enhancing the overall heat dissipation rate at high superheat.

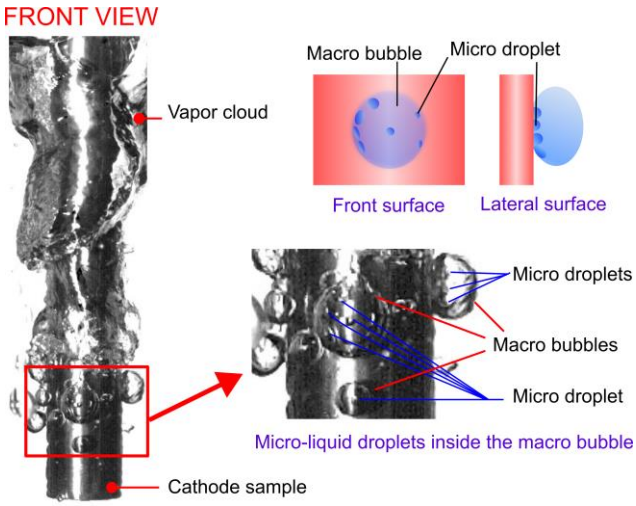

Fig. 16. High-speed visualization of enhanced boiling at the surface of repeatedly quenched cathode sample at 200 V.

5. Relevance of the outcomes from the present study

Based on the current research findings and insights, this section describes a practical application of mitigating thermal crisis in the cavity receiver used in direct steam generation (DSG) system employing beam down technology coupled with point focal concentration system.

DSG by beam down point focal concentration systems gained immense research interest as it allows for elimination of costly solar tower structures and heat transfer fluid, reduction in pumping power, high concentration range and shorter heat-traced piping [11]. Some characteristics examples of solar power plant with beam down technology are 100 kW_{th} beam down solar power plant at the Masdar Institute of Science and Technology [53], the thermochemical water-splitting reactor using beam-down technology at University of Miyazaki [54]. Due to high concentration range of beam down point focal concentration system the cavity receiver can reach a higher temperature which facilitates the generation of steam. Lorfing et al. [16] developed a lab scale solar boiler using the beam down point focal concentration system for steam generation.

Their system consists of conical cavity receiver, two water tanks: one for boiling process (main tank) and another for collecting overflow (secondary tank), feedwater inlet at the bottom of the main tank and outlet at the secondary tank, and steam outlet at the top of the main tank, as shown in the Fig. 17a and 17b. The solar energy is concentrated in a cavity receiver which is immersed in main tank, as shown in Fig. 17b, where the heat is used for steam generation. The heat transfer at the solar receiver is inherently transient as it directly dependent on the solar irradiation available at any given time. At high concentrated solar heat flux conditions, the receiver suffers from thermal crisis (film boiling) due to a sudden surge in receiver temperature. Film boiling limits the operating capacity of the receiver and affects its thermal efficiency. Further, prolonged film boiling at the surface of the cavity receiver leads to a thick and continuous vapour layer, as shown in Fig. 17c. Consequently, the heat dissipation rate decreases significantly, leading to the accumulation of input solar thermal energy within the cavity receiver. This, in turn, results in material degradation and eventually the complete breakdown of the solar receiver. Therefore, mitigating film boiling at the receiver is crucial for increasing the overall steam generation efficiency and avoiding the failure of the receiver.

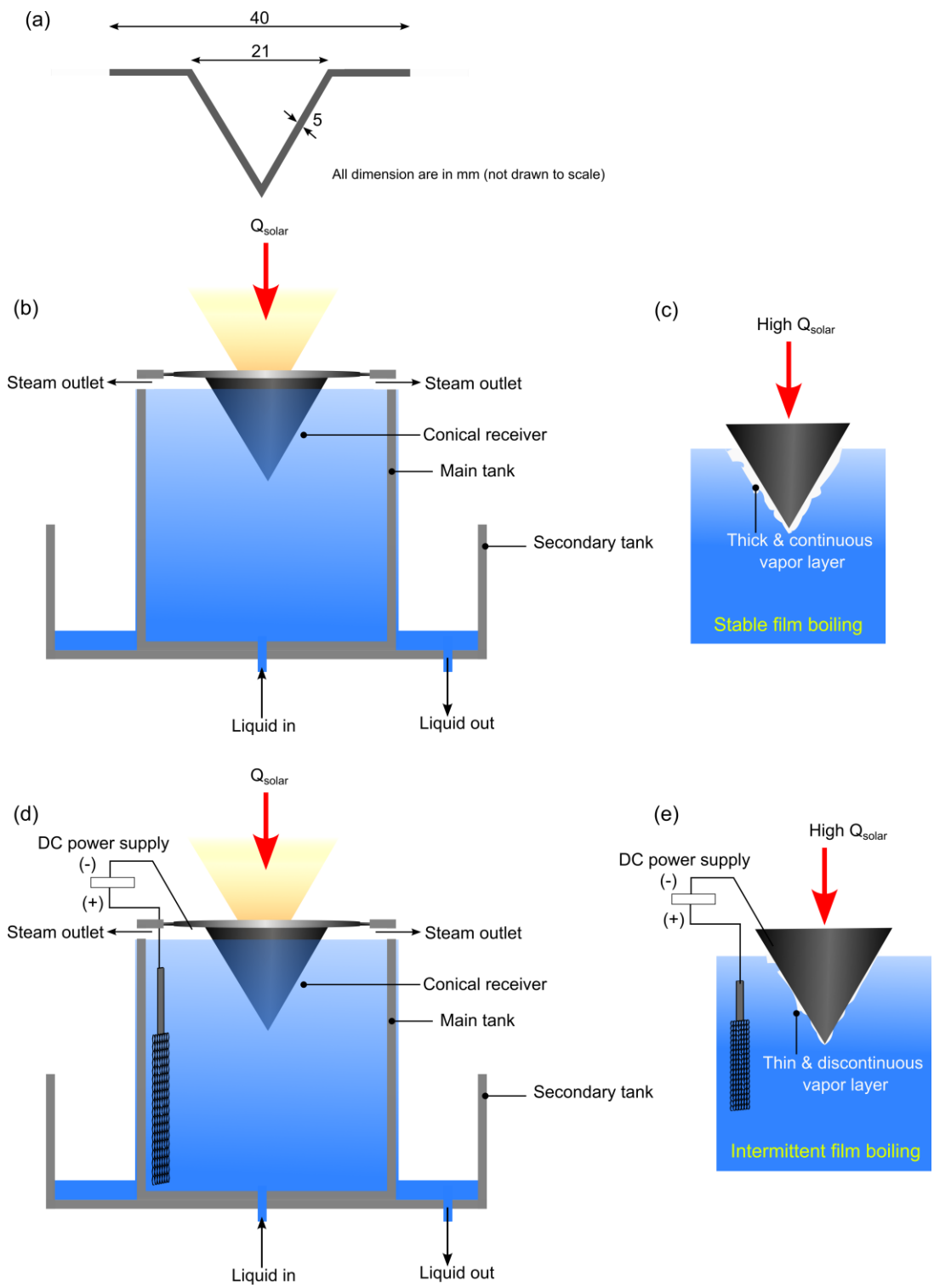

Fig. 17. Solar boiler: (a) cavity receiver dimensions, (b) solar boiler system, (c) stable film boiling at high concentrated heat flux conditions, (d) proposed modification to establish electric field, and (e) intermittent film boiling at high concentrated heat flux conditions.

The outcomes of the present study offer an effective solution to mitigate the film boiling under high heat flux conditions. The current experimental findings show that the application of electric field reduces the film boiling duration up to 55%. The maximum power utilised for this purpose

is 76 W, and the corresponding total energy consumed in our experiment is 0.63 Wh. Based on the current research findings and insights, a modified system design is proposed to mitigate film boiling at the solar cavity receiver. Fig. 17d illustrates the proposed modification to establish an electric field in a cavity receiver. The proposed design is simple and is associated with a low capital cost. The modification involves using the receiver as the cathode, the titanium (Ti) electrode as the anode, and a DC power supply. Importantly, the proposed design requires only localised modifications at the receiver module, such as provision for affixing the Ti electrode, establishing an electrical contact point on the receiver, and electrical insulation between the receiver and other components. SEM and EDS analyses (Fig. 13 and Fig. 15) have revealed that treating the receiver as a cathode leads to the production of hydrogen on the surface, which alleviates oxidation compared to other samples in continuous operation under dynamic (heating and cooling) conditions. As a result, the receiver's lifetime is extended, resulting in increased steam production with less maintenance. Further, the high corrosion resistance, lightweight, and excellent thermal and chemical stability of the Ti electrode will also ensure a longer lifetime. Consequently, the proposed design exhibits durability and good integration with existing infrastructure without any major customization or a comprehensive overhaul. These beneficial features of the proposed design point toward a favourable economic outlook and scalability. Some factors to be considered with regard to applicability include optimization of the distance between the anode and cathode, proper electrical insulation, and a ground fault protection system.

The mechanism of generating hydrogen bubbles at the receiver surface via electrolytic activity led to intermittent film boiling. This prevents the formation of continuous vapour film and reduces the film boiling duration, as shown in Fig. 17e.The current study also demonstrates that using an electric field increases the bubble nucleation density. This leads to transition and fully developed nucleate boiling happening at much higher temperatures with a faster heat transfer rate. Such enhanced heat transfer mechanisms aid in maximising the steam generation efficiency of the solar cavity receiver. Further efforts are necessary to improve the efficiency of electrolytic immersion cooling, and with the appropriate design modifications, this solution shows also good potential for use in additional applications.

6. Conclusions

We experimentally investigated the influence of a DC electric field, electrode polarity, and in-situ surface oxidation on immersion quenching heat transfer characteristics. The main findings are:

- The cooling curves of samples quenched in the presence of an electric field shift towards the left compared to the sample quenched without an electric field. The applied electric field increases T_{min} and accelerates the quenching for both electrode polarities (anode and cathode). The cathode sample displays a higher quenching efficiency than the anode sample. Overall, T_{min} increased from 268 °C to 301 °C at 200 V, contributing to 33% faster cooling of the cathode sample than the bare sample (0 V).
- Further, in the absence of an applied electric field, in-situ oxidation did not influence T_{min} in repeated quenching experiments. However, in-situ oxidation enhances the quenching heat transfer in the presence of an applied electric field, especially for the cathode sample. Overall, the in-situ oxidised cathode sample at 200 V exhibits a 55% reduction in film boiling duration, and T_{min} increased from 268 °C to 322 °C compared to the bare sample (0 V).
- The film boiling of a repeatedly quenched sample without an electric field exhibits a stable vapour layer with occasional oscillations. In contrast, the film boiling of a repeatedly quenched cathode sample at 200 V exhibits chaotic vapour layer behaviour with frequent oscillations. The enhanced heat transfer in the cathode sample is due to the combined action of electrostatic attraction and electrolytic activity at the sample surface. The selective in-situ oxidation at the cathode sample forms an oxide layer with nanoscale metal oxide particles and micro-cavities. The evolution of hydrogen and its adsorption in the oxide layer reduces the activation energy for bubble nucleation and improves the bubble density via liquid pumping.

As demonstrated experimentally, with the application of an electric field, the evolution of hydrogen and its adsorption at the sample surface facilitate transition and nucleate boiling at a much higher temperature range. This result can find many applications, especially in cases where high cooling rates are required. The implications in a specific solar application, used here as a demonstration/case study, were also considered, which led to the proposal of a revised design of the cavity of a solar receiver. The current research extends the barriers of transient two-phase cooling by simply taking advantage of the natural oxidation process during immersion quenching. The research findings and proposed mechanism offer a new, robust approach for mitigating thermal crises in high-energy density systems.

Nomenclature

c_p	Specific heat capacity (J/kg.K)	DI	Deionized
$\Delta H°$	Enthalpy change (J/mol)	EDS	Energy dispersive spectroscopy
i	Current time step	IHCA	Inverse heat conduction analysis
j	Number of temperature sensors	SEM	Scanning electron microscope
k	Thermal conductivity (W/m.K)	SS	Stainless steel
k_w	Equilibrium reaction constant	T_{min}	Minimum film boiling temperature
m	Global time steps	XRD	X-ray diffraction
q^c	Computed heat flux (W/m^2)		
$q''(t)$	Unknown heat flux (W/m^2)		
Δq	Correction term		
R	Universal gas constant (J/K.mol)		
r	Number of future time steps		
r_0	Radius of the sample (m)		
t	Time (s)		
$T(r,z,t)$	Instantaneous temperature (°C)		
$T_{meas}(t)$	Time-dependent measured temperature (°C)		
$T_{initial}$	Initial temperature (°C)		

Greek symbols

ρ	Density (kg/m^3)
$\emptyset$	Sensitivity coefficient
ϵ	Change in computed temperature

Abbreviations

CHF	Critical heat flux

Acknowledgement

The authors acknowledge the financial support received from CRG-SERB [CRG/2022/005638], and SIRE- SERB [SIR/2022/001319], India. The authors thank the Department of Science and Technology, Government of India for supporting this work under the scheme FIST (No. SR/ FST/ETI-388/2015). This work was also supported by the UK Engineering and Physical Sciences Research Council (EPSRC) [grant number EP/T03338X/1]. For the purpose of Open Access, the authors have applied a CC BY public copyright licence to any Author Accepted Manuscript version arising from this submission.

References

[1] Khosla R, Miranda ND, Trotter PA, Mazzone A, Renaldi R, McElroy C, et al. Cooling for sustainable development. Nat Sustain 2021;4:201–8. https://doi.org/10.1038/s41893-020-00627-w.

[2] Huo X, Yang L, Li DHW, Zhai Y, Lou S. A novel index for assessing the climate potential of free-running buildings based on the acceptable upper limits of thermal comfort models across China. Energy Convers Manag 2023;278:116692. https://doi.org/https://doi.org/10.1016/j.enconman.2023.116692.

[3] Jeong H, Byun S, Kim DR, Lee K-S. Power optimization for defrosting heaters in household refrigerators to reduce energy consumption. Energy Convers Manag 2021;237:114127. https://doi.org/https://doi.org/10.1016/j.enconman.2021.114127.

[4] Zaki OM, Mohammed RH, Abdelaziz O. Separate sensible and latent cooling technologies: A comprehensive review. Energy Convers Manag 2022;256:115380. https://doi.org/https://doi.org/10.1016/j.enconman.2022.115380.

[5] Chu S, Majumdar A. Opportunities and challenges for a sustainable energy future. Nature 2012;488:294–303. https://doi.org/10.1038/nature11475.

[6] Stephenson J, Barton B, Carrington G, Gnoth D, Lawson R, Thorsnes P. Energy cultures: A framework for understanding energy behaviours. Energy Policy 2010;38:6120–9. https://doi.org/https://doi.org/10.1016/j.enpol.2010.05.069.

[7] Huang Y, Xiao X, Kang H, Lv J, Zeng R, Shen J. Thermal management of polymer electrolyte membrane fuel cells: A critical review of heat transfer mechanisms, cooling approaches, and advanced cooling techniques analysis. Energy Convers Manag

2022;254:115221. https://doi.org/https://doi.org/10.1016/j.enconman.2022.115221.

[8] Cirocco L, Pudney P, Riahi S, Liddle R, Semsarilar H, Hudson J, et al. Thermal energy storage for industrial thermal loads and electricity demand side management. Energy Convers Manag 2022;270:116190. https://doi.org/https://doi.org/10.1016/j.enconman.2022.116190.

[9] Sofu T. A review of inherent safety characteristics of metal alloy sodium-cooled fast reactor fuel against postulated accidents. Nucl Eng Technol 2015;47:227–39. https://doi.org/https://doi.org/10.1016/j.net.2015.03.004.

[10] Droin J-B, Marie N, Bachrata A, Bertrand F, Merle E, Seiler J-M. Physical tool for Unprotected Loss Of Flow transient simulations in a Sodium Fast Reactor. Ann Nucl Energy,2017;106:195–210. https://doi.org/https://doi.org/10.1016/j.anucene.2017.03.035.

[11] Bellos E. Progress in beam-down solar concentrating systems. Prog Energy Combust Sci 2023;97:101085. https://doi.org/https://doi.org/10.1016/j.pecs.2023.101085.

[12] Al Kindi AA, Sapin P, Pantaleo AM, Wang K, Markides CN. Thermo-economic analysis of steam accumulation and solid thermal energy storage in direct steam generation concentrated solar power plants. Energy Convers Manag 2022;274:116222. https://doi.org/https://doi.org/10.1016/j.enconman.2022.116222.

[13] Ferchichi S, Kessentini H, Morales-Ruiz S, Rigola J, Bouden C, Oliva A. Thermal and fluid dynamic analysis of Direct Steam Generation Parabolic Trough Collectors. Energy Convers Manag 2019;196:467–83. https://doi.org/https://doi.org/10.1016/j.enconman.2019.05.107.

[14] Yang H, Wang Q, Huang Y, Gao G, Feng J, Li J, et al. Novel parabolic trough power system integrating direct steam generation and molten salt systems: Preliminary thermodynamic study. Energy Convers Manag 2019;195:909–26. https://doi.org/https://doi.org/10.1016/j.enconman.2019.05.072.

[15] Mohite SJ, Reddy KS. Optical and thermal analysis of solar parabolic dish cavity receiver system for hydrogen production using deep learning. Energy Convers Manag 2023;292:117415. https://doi.org/https://doi.org/10.1016/j.enconman.2023.117415.

[16] Lorfing D, Olives R, Falcoz Q, Guillot E, Le Men C, Ahmadi A. Design and performance of a new type of boiler using concentrated solar flux. Energy Convers

Manag 2021;249:114835. https://doi.org/https://doi.org/10.1016/j.enconman.2021.114835.

[17] Javidan M, Moghadam AJ. Experimental investigation on thermal management of a photovoltaic module using water-jet impingement cooling. Energy Convers Manag 2021;228:113686. https://doi.org/https://doi.org/10.1016/j.enconman.2020.113686.

[18] Chen H, Wang Y, Yang H, Badiei A, Li G. Experimental investigation and exergy analysis of a high concentrating photovoltaic system integrated with spray cooling. Energy Convers Manag 2022;268:115957. https://doi.org/https://doi.org/10.1016/j.enconman.2022.115957.

[19] Zhang L, Duan Q, Meng X, Jin K, Xu J, Sun J, et al. Experimental investigation on intermittent spray cooling and toxic hazards of lithium-ion battery thermal runaway. Energy Convers Manag 2022;252:115091. https://doi.org/https://doi.org/10.1016/j.enconman.2021.115091.

[20] Abo-Zahhad EM, Ookawara S, Radwan A, Memon S, Yang Y, El-Kady MF, et al. Flow boiling in a four-compartment heat sink for high-heat flux cooling: A parametric study. Energy Convers Manag 2021;230:113778. https://doi.org/https://doi.org/10.1016/j.enconman.2020.113778.

[21] Wang Y-F, Wu J-T. Thermal performance predictions for an HFE-7000 direct flow boiling cooled battery thermal management system for electric vehicles. Energy Convers Manag 2020;207:112569. https://doi.org/https://doi.org/10.1016/j.enconman.2020.112569.

[22] Radwan A, Ookawara S, Mori S, Ahmed M. Uniform cooling for concentrator photovoltaic cells and electronic chips by forced convective boiling in 3D-printed monolithic double-layer microchannel heat sink. Energy Convers Manag 2018;166:356–71. https://doi.org/https://doi.org/10.1016/j.enconman.2018.04.037.

[23] Zhang S, Jiang X, Li Y, Chen G, Sun Y, Tang Y, et al. Extraordinary boiling enhancement through micro-chimney effects in gradient porous micromeshes for high-power applications. Energy Convers Manag 2020;209:112665. https://doi.org/https://doi.org/10.1016/j.enconman.2020.112665.

[24] Lim YS, Hung YM. Anomalously enhanced light-emitting diode cooling via nucleate boiling using graphene-nanoplatelets coatings. Energy Convers Manag

2021;244:114522. https://doi.org/https://doi.org/10.1016/j.enconman.2021.114522.

[25] Khan SA, Sezer N, Ismail S, Koç M. Design, synthesis and nucleate boiling performance assessment of hybrid micro-nano porous surfaces for thermal management of concentrated photovoltaics (CPV). Energy Convers Manag 2019;195:1056–66. https://doi.org/https://doi.org/10.1016/j.enconman.2019.05.068.

[26] Roh H-S. Heat transfer mechanisms in pool boiling. Int J Heat Mass Transf 2014;68:332–42. https://doi.org/https://doi.org/10.1016/j.ijheatmasstransfer.2013.09.037.

[27] Bahiraei M, Heshmatian S. Electronics cooling with nanofluids: A critical review. Energy Convers Manag 2018;172:438–56. https://doi.org/https://doi.org/10.1016/j.enconman.2018.07.047.

[28] Inbaoli A, S SKC, Jayaraj S. A review on techniques to alter the bubble dynamics in pool boiling. Appl Therm Eng 2022;214:118805. https://doi.org/10.1016/j.applthermaleng.2022.118805.

[29] Chu H, Xu N, Yu X, Jiang H, Ma W, Qiao F. Review of surface modification in pool boiling application: Coating manufacturing process and heat transfer enhancement mechanism. Appl Therm Eng 2022;215:119041. https://doi.org/https://doi.org/10.1016/j.applthermaleng.2022.119041.

[30] Fan L-W, Li J-Q, Su Y-Y, Wang H-L, Ji T, Yu Z-T. Subcooled Pool Film Boiling Heat Transfer From Spheres With Superhydrophobic Surfaces: An Experimental Study. J Heat Transfer 2015;138. https://doi.org/10.1115/1.4031303.

[31] Liang G, Mudawar I. Review of nanoscale boiling enhancement techniques and proposed systematic testing strategy to ensure cooling reliability and repeatability. Appl Therm Eng 2021;184:115982. https://doi.org/10.1016/j.applthermaleng.2020.115982.

[32] Li S, Furberg R, Toprak MS, Palm B, Muhammed M. Nature-Inspired Boiling Enhancement by Novel Nanostructured Macroporous Surfaces. Adv Funct Mater 2008;18:2215–20. https://doi.org/https://doi.org/10.1002/adfm.200701405.

[33] Sujith Kumar CS, Udaya Kumar G, Mata Arenales MR, Hsu C-C, Suresh S, Chen P-H. Elucidating the mechanisms behind the boiling heat transfer enhancement using nano-structured surface coatings. Appl Therm Eng 2018;137:868–91. https://doi.org/https://doi.org/10.1016/j.applthermaleng.2018.03.092.

[34] Ng BT, Hung YM, Tan MK. Acoustically-controlled Leidenfrost droplets. J Colloid Interface Sci 2016;465:26–32. https://doi.org/https://doi.org/10.1016/j.jcis.2015.11.047.

[35] Celestini F, Kirstetter G. Effect of an electric field on a Leidenfrost droplet. Soft Matter 2012;8:5992–5. https://doi.org/10.1039/C2SM25656H.

[36] Shahriari A, Hermes M, Bahadur V. Electrical control and enhancement of boiling heat transfer during quenching. Appl Phys Lett 2016;108:91607. https://doi.org/10.1063/1.4943230.

[37] Song Y, Cha H, Liu Z, Seong JH, Zhang L, Preston DJ, et al. Alteration of pool boiling heat transfer on metallic surfaces by in situ oxidation. Int J Heat Mass Transf 2022;185:122320. https://doi.org/https://doi.org/10.1016/j.ijheatmasstransfer.2021.122320.

[38] Ebrahim SA, Alat E, Sohag FA, Fudurich V, Chang S, Cheung F-B, et al. Effects of Substrate Materials and Surface Conditions on the Minimum Film-Boiling Temperature. Nucl Technol 2019;205:226–38. https://doi.org/10.1080/00295450.2018.1490122.

[39] Lee CY, Chun TH, In WK. Effect of change in surface condition induced by oxidation on transient pool boiling heat transfer of vertical stainless steel and copper rodlets. Int J Heat Mass Transf 2014;79:397–407. https://doi.org/https://doi.org/10.1016/j.ijheatmasstransfer.2014.08.030.

[40] Cho HJ, Mizerak JP, Wang EN. Turning bubbles on and off during boiling using charged surfactants. Nat Commun 2015;6:1–7.

[41] Cheng H-C, Lin H-C, Chen P-H. Boiling heat transfer enhancement over copper tube via electrolytic and electrostatic effects. Appl Therm Eng 2021;199:117584. https://doi.org/https://doi.org/10.1016/j.applthermaleng.2021.117584.

[42] Inbaoli A, Sujith Kumar CS, Jayaraj S. Experimental investigation on the effect of additives on different orientations of Al6061 cylindrical sample during immersion quenching. Appl Therm Eng 2022;204:118030. https://doi.org/https://doi.org/10.1016/j.applthermaleng.2021.118030.

[43] Babu K, Prasanna Kumar TS. Effect of CNT concentration and agitation on surface heat flux during quenching in CNT nanofluids. Int J Heat Mass Transf 2011;54:106–17. https://doi.org/https://doi.org/10.1016/j.ijheatmasstransfer.2010.10.003.

[44] Kumar TP. Coupled analysis of surface heat flux, microstructure evolution, and hardness during immersion quenching of a medium carbon steel in plant conditions. Mater Perform Charact 2012;1:MPC104477.

[45] Lee SG, Kaviany M, Lee J. Role of quenching method on cooling rate and microstructure of steels: Variations in coolant and its flow arrangement. Int J Heat Mass Transf 2022;189:122702. https://doi.org/https://doi.org/10.1016/j.ijheatmasstransfer.2022.122702.

[46] Chen X, Zhang L, Jie X, Li Y, Huang X. Quenching characteristics of glycerol solution as a potential new quenchant. Int J Heat Mass Transf 2017;109:209–14. https://doi.org/https://doi.org/10.1016/j.ijheatmasstransfer.2017.02.013.

[47] Blackwell B, Beck J V. A technique for uncertainty analysis for inverse heat conduction problems. Int J Heat Mass Transf 2010;53:753–9. https://doi.org/https://doi.org/10.1016/j.ijheatmasstransfer.2009.10.014.

[48] Dong K, Ding S, Chen D, Wu D, Deng J, Liu H, et al. Experimental investigation on minimum film boiling temperature during reflooding in multi-rectangular narrow channels. Int J Heat Mass Transf 2021;178:121635. https://doi.org/https://doi.org/10.1016/j.ijheatmasstransfer.2021.121635.

[49] Babu K, Prasanna Kumar TS. Mathematical Modeling of Surface Heat Flux During Quenching. Metall Mater Trans B 2010;41:214–24. https://doi.org/10.1007/s11663-009-9319-y.

[50] Olivares-Ramírez JM, Campos-Cornelio ML, Uribe Godínez J, Borja-Arco E, Castellanos RH. Studies on the hydrogen evolution reaction on different stainless steels. Int J Hydrogen Energy 2007;32:3170–3. https://doi.org/https://doi.org/10.1016/j.ijhydene.2006.03.017.

[51] Kim H, DeWitt G, McKrell T, Buongiorno J, Hu L. On the quenching of steel and zircaloy spheres in water-based nanofluids with alumina, silica and diamond nanoparticles. Int J Multiph Flow 2009;35:427–38. https://doi.org/https://doi.org/10.1016/j.ijmultiphaseflow.2009.02.004.

[52] Xiong J, Wang Z, Xiong P, Lu T, Yang Y. Experimental investigation on transient boiling heat transfer during quenching of fuel cladding surfaces. Int J Heat Mass Transf 2020;148:119131.

https://doi.org/https://doi.org/10.1016/j.ijheatmasstransfer.2019.119131.

[53] Mokhtar M, Meyers SA, Armstrong PR, Chiesa M. Performance of a 100 kWth Concentrated Solar Beam-Down Optical Experiment. J Sol Energy Eng 2014;136. https://doi.org/10.1115/1.4027576.

[54] Kodama T, Gokon N, Matsubara K, Yoshida K, Koikari S, Nagase Y, et al. Flux Measurement of a New Beam-down Solar Concentrating System in Miyazaki for Demonstration of Thermochemical Water Splitting Reactors. Energy Procedia 2014;49:1990–8. https://doi.org/https://doi.org/10.1016/j.egypro.2014.03.211.